

/STUDIES ON THE STOCHASTIC BEHAVIOR
OF THE GAS-SOLID FLUIDIZED BED/

by

YEE-WEI HUANG

B.S., National Taiwan University, 1980

A MASTER'S THESIS

submitted in partial fulfillment of the
requirements for the degree

MASTER OF SCIENCE

College of Engineering

KANSAS STATE UNIVERSITY
Manhattan, Kansas

1984

Approved by:

L. J. Flan
Major Professor

LD
3668
-T-
4984
1182
2.2

ALL202 961279

TABLE OF CONTENTS

	<u>Page</u>
LIST OF FIGURES.....	i
LIST OF TABLES.....	iv
ACKNOWLEDGMENTS.....	v
CHAPTER 1. INTRODUCTION.....	1-1
CHAPTER 2. LITERATURE REVIEW.....	2-1
2.1 Stochastic Modeling of the Bubble Coalescence and Breakage...2-1	
2.2 Screen Effect on a Fluidized Bed.....2-3	
2.3 Temperature Effect on a Fluidized Bed.....2-4	
CHAPTER 3. STOCHASTIC MODELING OF BUBBLE COALESCENCE AND BREAKAGE BY USING THE MASTER EQUATION.....	3-1
3.1 System Description.....	3-3
3.2 Master Equation Formulation.....	3-3
3.3 Master Equation Expansion.....	3-10
3.4 Extension to an Open System.....	3-16
3.5 A Case Study: Two-Bubble-Size System.....	3-17
3.6 Discussion.....	3-25
NOTATION.....	3-27
APPENDIX A. Conversion of Equation (8) into a Continuous Form, Equation (12).....	3-33
APPENDIX B. Rearrangement of Equation (28) to a Compact Form, Equation (30).....	3-36
APPENDIX C. Derivation of Equations (31) and (32).....	3-40
APPENDIX D. Solution for Equation (45).....	3-45

APPENDIX E. Steady-State Solution for Equation Set (37a)	<u>Page</u>
and (37b).....	3-47
APPENDIX F. Solution for Constants c_1 and c_3 in Equation (71)....	3-48
CHAPTER 4. PRESSURE FLUCTUATIONS IN A GAS-SOLID FLUIDIZED BED	
WITH A SCREEN.....	4-1
4.1 Experimental.....	4-2
Facilities.....	4-2
Procedure.....	4-3
4.2 Results and Discussion.....	4-4
NOTATION.....	4-11
APPENDIX A. Pre-experimental Calibration and Test Run.....	4-28
APPENDIX B. Auto-correlation Function and Power Spectral	
Density Function.....	4-36
CHAPTER 5. STATISTICAL ANALYSIS OF TEMPERATURE EFFECTS ON PRESSURE	
FLUCTUATIONS IN A GAS-SOLID FLUIDIZED BED.....	5-1
5.1 Experimental.....	5-2
Facilities.....	5-2
Procedure.....	5-4
5.2 Results and Discussion.....	5-5
NOTATION.....	5-12
CHAPTER. 6 CONCLUSIONS AND RECOMMENDATIONS.....	6-1
LITERATURE CITED.....	L-1

LIST OF FIGURES

Page

CHAPTER 3.

Fig. 3-1.	Logistic flow chart for stochastic modeling.	3-29
Fig. 3-2.	P-{n}-t relationship for illustrating the bubble size distribution in a dispersed bubbling system.	3-30
Fig. 3-3.	Paths entering and leaving a reference state {n} in a dispersed bubbling system.	3-31
Fig. 3-4.	Discrete function set {n} and its continuous function form n(V).	3-32

CHAPTER 4.

Fig. 4-1.	Experimental setup	4-15
Fig. 4-2.	Hole layout of the distributor	4-16
Fig. 4-3.	Screen effect on the average pressure drop through the fluidized bed.	4-17
Fig. 4-4.	Pressure fluctuation signal from the fluidized bed without screen at $U/U_{mf} = 3$	4-18
Fig. 4-5.	Pressure fluctuation signal from the fluidized bed with a 8x8 mesh screen at $U/U_{mf} = 3$	4-19
Fig. 4-6.	Pressure fluctuation signal of the fluidized bed with a 12 x 14 mesh screen at $U/U_{mf} = 3$	4-20
Fig. 4-7.	Pressure fluctuation signal of the fluidized bed with a 20 x 20 mesh screen at $U/U_{mf} = 3$	4-21
Fig. 4-8.	Auto-correlation functions of the pressure fluctuation signals from the fluidized bed at $U/U_{mf} = 3.1$	4-22
	(a) without screen	
	(b) with a 8x8 mesh screen	
	(c) with a 12x14 mesh screen	
	(d) with a 20x20 mesh screen	
	(Reproduced from the X-Y plotter; CPA attenuation = 15 db.)	

Fig. 4-9.	Power spectral density functions of the pressure fluctuation signals from the fluidized bed bed at $U/U_{mf} = 3.1$. . .	4-23
	(a) without screen	
	(b) with a 8x8 mesh screen	
	(c) with a 12x14 mesh screen	
	(d) with a 20x20 mesh screen	
	(Reproduced from the X-Y plotter with peak values determined by the oscilloscope cursor.)	
Fig. 4-10.	Screen effect on the fluidized bed expansion.	4-24
Fig. 4-11.	Pressure fluctuation signal from the fluidized bed with a 20x20 mesh screen at $U/U_{mf} = 2.9$ exhibiting a periodic wave superimposed on the random fluctuations	4-25
Fig. 4-12.	Screen effect on the major frequency of pressure fluctuations	4-26
Fig. 4-13.	Screen effect on the variance of pressure fluctuations. . .	4-27
Fig. 4-A.1.	Calibration curve of the strip chart recorder	4-33
Fig. 4-A.2.	Calibration curve of the X-Y plotter.	4-34
Fig. 4-A.3.	Pressure drop versus linear air velocity curve for determination of the minimum fluidization velocity. . . .	4-35

CHAPTER 5

Fig. 5-1.	Experimental setup.	5-17
Fig. 5-2.	Configuration of the pressure probe	5-18
Fig. 5-3.	Dynamic approach to determine the minimum fluidization velocity.	5-19
Fig. 5-4.	Relationship between $\ln V_{mf}$ and $\ln T$	5-20
Fig. 5-5.	Relationship between u_{mf} and T	5-21
Fig. 5-6.	Relationship between f_m and T with u_0/u_{mf} as the parameter . .	5-22
Fig. 5-7.	Relationship between f_m and u_0/u_{mf} with T as the parameter (Low temperature range)	5-23

	<u>Page</u>
Fig. 5-8. Relationship between f_n and u_0/u_{mf} with T as the parameter (High temperature range).	5-24
Fig. 5-9. Relationship between Amp and u_0/u_{mf} with T as the parameter	5-25
Fig. 5-10. Relationship between Amp and T with u_0/u_{mf} as the parameter	5-26

LIST OF TABLES

Page

CHAPTER 4.

Table 4-1. Experimental results showing the screen effect on the major frequency of pressure fluctuations in the fluidized bed.	4-13
Table 4-2. Experimental results showing the screen effect on the variance of pressure fluctuations in the fluidized bed .	4-14
Table 4-A.1. Pre-experimental calibration data for pressure-voltage conversion in using CPA and X-Y plotter (X-Y plotter sensitivity setting = 50 mV/cm)	4-32

CHAPTER 5.

Table 5-1. Temperature effect on the minimum fluidication velocity.	5-14
Table 5-2. Temperature effect on the major frequencies of pressure fluctuations at different air velocities	5-15
Table 5-3. Temperature effect on the amplitudes of pressure fluctuations at different air velocities	5-16

ACKNOWLEDGMENTS

The author wishes to express his gratitude and sincere thanks to Dr. L. T. Fan, Professor and Head of Chemical Engineering Department at Kansas State University for his continuous guidance throughout the preparation of this thesis. Thanks are also due to the members of the advisory committee, Dr. Larry A. Glasgow, Associate Professor of Chemical Engineering and Dr. Raja F. Nassar, Professor of Statistics, Kansas State University.

The author also wishes to express his appreciation to the following persons for their assistance in this work.

Dr. N. Yutani, Chemical Engineering Department of Tokyo University of Agriculture and Technology, Tokyo, Japan, for his valuable suggestions and criticisms on improving the experimental techniques.

Dr. K. C. Kim, Chemical Engineering Department of Ulsan Institute of Technology, Ulsan, Korea, and Mr. J. C. Song, Chenguang Research Institute of Chemical Industry, Sichuan, China, for their help in the experimental works.

Mr. Rodney Fox for his consultation during the development of the master equation formulation.

Mr. D. Morey and Mr. D. Neogi for their fabricating the apparatus used in this work.

The research assistantship awarded by the Department of Chemical Engineering, Kansas State University for the academic years 1982-1984 is also gratefully acknowledged.

The author dedicates this work to his parents, Mr. and Mrs. M. C. Huang. Without their love and encouragement, this work could never have been accomplished.

CHAPTER 1

INTRODUCTION

Fluidized beds are of considerable importance to energy resources conversion and energy conservation in view of their versatile applications in different operations, such as coal gasification, coal liquefaction, oil shale retorting, solid fuel combustion, biomass pyrolysis, catalytic hydrocarbon synthesis, and waste heat recovery. The behavior of a fluidized bed has been investigated extensively by numerous researchers since the early 1940's. In spite of this and the fact that fluidized beds have been successfully applied to many processes, (see, e.g., Kuni and Levenspiel, 1969), their characteristics, especially local, microscopic, mesoscopic or dynamic characteristics, are yet to be fully understood because of their complexity and because of the lack of suitable techniques and facilities for studying them.

To characterize a fluidized bed, it is necessary to have a thorough understanding of the hydrodynamics or aerodynamics of the bed. The hydrodynamics of the bed are known to be interrelated to fluctuations of pressure or porosity around their mean values over the bed. It is worth mentioning that fluctuations in parameters of the physical phenomena in a process often reveal important characteristics of the system (see, e.g., Prigogine and Stengers, 1984). The nature of pressure or porosity fluctuations in a fluidized bed is a complex function of various factors, including particle properties, bed configuration, pressure, temperature, external noises, and properties and flow conditions of the fluidizing fluid. Most of these factors affecting the hydrodynamics of the bed are stochastic in nature, and indeed considerable effort has been spent to study them from

stochastic or statistical points of view (see, e.g., Orcutt and Carpenter, 1971; Buker et al., 1977); however, the majority of the so-called stochastic investigations conducted in the past resorted to somewhat ad hoc approaches.

It is the objective of this work to study statistically and stochastically the hydrodynamic properties of a gas-solid fluidized bed. The emphases are on the topics of bubble coalescence and breakage phenomena as well as the screen and temperature effects on the bed performances. In addition to the present chapter, this thesis contains five chapters. Chapter 2 reviews the literature on three different aspects of fluidized-bed hydrodynamics, including the bubble coalescence and breakage phenomena, screen effect, and temperature effect. Chapter 3 deals with the modeling of bubble coalescence and breakage in a dispersed system by the master equation approach. The proposed formulation can be readily extended to the modeling of bubbling in a fluidized bed. In Chapter 4, the screen effect on the behavior of a fluidized bed is discussed. Chapter 5 is concerned with the hydrodynamics of a fluidized bed at elevated temperature. The concluding remarks and recommendations for future work are contained in the last chapter, Chapter 6.

CHAPTER 2

LITERATURE REVIEW

This chapter reviews the literature on three different aspects of the fluidized bed, namely, the stochastic modeling of the bubble coalescence and breakage in a fluidized bed, the screen effect on a fluidized bed, and the temperature effect on a fluidized bed.

2.1 STOCHASTIC MODELING OF THE BUBBLE COALESCENCE AND BREAKAGE

The bubble coalescence and breakage phenomena extensively influence the hydrodynamic properties of a fluidized bed. These phenomena have been observed to be stochastic in nature (see, e.g., Orcutt and Carpenter, 1971; Argyriou et al., 1971; Buckur et al., 1977); however, it appears that only limited effort has been made toward studying them from a stochastic point of view. In this section, we first examine some previous attempts at modeling bubble coalescence and breakage in dispersed systems in general. This is followed by a review of the publications specifically concerned with these phenomena in fluidized beds. The review focuses on those works emphasizing mathematical modeling.

Valentas and Amundson (1966) were among the earliest workers to mathematically model the coalescence and breakage of bubbles in a continuous dispersed-phase system. They resorted to a deterministic population balance approach to determine the steady-state distribution of bubble sizes; however, their model can not be used in a predictive manner because of the lack of information on the frequencies of coalescence and breakage. To remedy this situation, various groups of workers (e.g., Ramkrishna, 1974; Bajpai et al., 1976; Coulaloglou and Tavlarides, 1977)

have extended the population balance equation specifically to agitated liquid-liquid dispersed systems in which the bubble coalescence and breakage frequencies can be empirically evaluated. Argyriou et al., (1971) have presented a population balance formulation to describe the bubble growth in a fluidized bed following the mathematical framework proposed by Hulburt and Katz (1964). Note that all these approaches are essentially deterministic, based on the conservation of the bubble volume, and can not realistically describe the stochastic nature of a fluidized bed. Shah et al. (1977) resorted to a simulation technique in solving the population balance equation to analyze the dynamics of bubble populations in a gas fluidized bed. Ligon and Amundson (1981 a,b) have developed stochastic models to investigate the significance of the fluctuating nature of fluidized beds on reactor performance. The fluctuating bubble size distribution within the bed is simulated by stochastic mass and heat transfer coefficients. Ho et al. (1983) have proposed a stochastic renewal counting process to model the bubble formation.

The so-called master equation is the probability balance equation of a Markov process (van Kampen, 1981). Fox and Fan (1984) have successfully applied this formulation to the analysis of the residence time distributions in continuous stirred tank reactors. Their work indicates that the master equation approach is worth exploiting for stochastically modeling dispersed systems in general, and fluidized beds in particular.

2.2 SCREEN EFFECT ON A FLUIDIZED BED

The heterogeneity caused by bubbling, slugging, and channeling in a fluidized bed is undesirable because they reduce the extent of fluid-solid contact and, thus, the efficiency of the process (Bakker and Heertjes, 1958, 1960). It has been suggested that bubbles, slugs, and channels might be reduced by inserting a screen or other mechanical devices in the bed (Massimilla, *et al.*, 1956). Although the screen prevents channeling and slugging, it causes other concomitant effects, e.g., hindering the heat and mass exchanges among various regions in the bed. The effects of screen insertion on the fluidized bed behavior were investigated by different methods. Massimilla *et al.* (1960) carried out a photographic study of the flow pattern in a fluidized bed with screen baffles, and Bailie *et al.* (1963) used the gamma-ray attenuation technique to investigate the longitudinal solid density distribution in a gas-solid screen fluidized bed.

The effect of screen becomes pronounced as the number and fineness of the screens are increased (Winter, 1968). The root mean square values of pressure fluctuations are lower for a packed fluidized bed than those of the same fluidized bed with no packing. Furthermore, a maximum is observed on a plot of the root mean square vs. flow rate for each packing; when no packing is used, the root mean square values increase continuously with the gas flow rate (Kang *et al.*, 1967). On the other hand, it has also been observed that gas channeling and holdup of particles in packing interstices exist in a packed bed (Sutherland *et al.*, 1963).

Several investigators (Sutherland et al., 1963; Kang et al., 1967; Winter, 1968) examined experimentally the effect of open and cylindrical packings and screen inserts on the stability of the gas-solids fluidized bed. The diameter of the open and cylindrical packings and the opening of screens employed were much larger than the average diameter of particles.

To enhance our fundamental understanding of the effect of screen packing on the performance of the gas-solid fluidized bed in terms of pressure fluctuations, it is highly desirable that a bed with the simplest possible configuration be examined; in other words, a bed with a single screen installed across the entire section of the bed should be investigated.

2.3 TEMPERATURE EFFECT ON A FLUIDIZED BED

Although the majority of fluidized-bed processes are operated at elevated temperatures, relatively little effort has been spent to investigate the hydrodynamic behavior of fluidized beds at such temperatures. Various aspects of the fluidized bed behavior, such as the minimum fluidization velocity, the bubble frequency, and the apparent bed viscosity, change significantly with temperature (Mii et al., 1973); however, most of the research in the past only emphasized the variation of minimum fluidization velocity (Singh et al., 1973; Broughton, 1974; Saxena and Vogel, 1977; Desai et al., 1977; Doheim and Collinge, 1978; Sovboda and Hartman, 1981a,b; Batterfill et al., 1982). Yoshida et al. (1975) were among the first to publish data on bubble sizes at high temperature. Geldart and Kapoor (1976) studied the temperature effect on the minimum bubbling velocity. Yamazaki et al. (1984) investigated the characteristics of slugging at elevated temperatures.

Research efforts on the dynamic behavior of fluidized beds, such as pressure fluctuations, at high temperatures have indeed been limited. Svoboda et al. (1983) analyzed the pressure fluctuations in a gas-solid fluidized bed at elevated temperatures. Their results show a significant temperature effect on the pressure fluctuations in terms of the major frequency and amplitude; however, only a limited number of data are presented by them. Furthermore, since the pressure and temperature are inversely related to each other for a gas, the temperature effect on the fluidized bed behavior can be deduced from the pressure effect (Weimer and Quarderer, 1983; Knowlton and Hirsan, 1984).

CHAPTER 3

STOCHASTIC MODELING OF BUBBLE COALESCENCE AND BREAKAGE
BY USING THE MASTER EQUATION

The bubble coalescence and breakage phenomena are important in studying a multi-phase dispersed system in view of their direct influence on the system dynamics and behavior. Specifically, it is well known that the knowledge of the evolution of the bubble size distribution is of significance for predicting the parameters of the system, such as the interfacial area and the rates of heat and mass transfer between phases, which, in turn, govern the system performance. While the bubble coalescence and breakage are stochastic in nature, all the previous attempts to model the phenomena resorted to the deterministic approach, or at best, to a somewhat ad hoc stochastic approximation. In this chapter, a comprehensive and systematic methodology, which is capable of not only describing the macroscopic (deterministic) component of bubble coalescence and breakage but also recovering the microscopic or mesoscopic (stochastic) information about the bubble population is developed. The methodology is known as the master equation formulation followed by its expansion (van Kampen, 1981).

For simplicity in stochastic modeling, an assumption of the Markov property can be imposed. This often gives rise to the absolute probability balance (or the Master equation) of the fluctuating variables being modeled. Expansion of this equation around the macroscopic value of a variable leads

to both a macroscopic (deterministic) expression (population balance) and a stochastic diffusion equation characterizing the dispersion around the macroscopic mean value. A logistic flow chart of the stochastic modeling work is presented in Fig. 3-1. It will be shown, by use of the master equation expansion, that we can first obtain the bubble population balance equation representing the macroscopic profile. In addition, a Fokker-Planck equation is generated from the expansion, recovering the mesoscopic information about the bubble size distribution. Thus, a fairly complete description of a stochastically behaving system is achieved by resorting to both the population balance and Fokker-Planck equations. This is illustrated with a simple example of a two-bubble-size batch system for which the analytical expression is attainable.

3.1 SYSTEM DESCRIPTION

Consider a multi-phase closed system; the probability for this system to have a bubble size distribution of $\{n\} = \{n_1, n_2, n_3, \dots, n_i\}$ at time t is denoted as $P(\{n\}, t)$. Figure 3-2 depicts a $P(\{n\})-t$ relationship. $P(\{n\}, t)$ signifies the probability that the system, at an arbitrary time t , consists of n_1 (number of) bubbles of size lc , n_2 bubbles of size $2c$, and so on, where n_i 's are random numbers and c is an infinitesimal volume element. The following assumptions are imposed to derive the master equation of the system;

- (1) The time interval, Δt , is chosen sufficiently small so that no more than one transition, bubble coalescence or breakage, is observed during this time interval.
- (2) Coalescence is binary; a target bubble emerges at the expense of two and only two smaller size source bubbles. Higher order collisions can be treated as binary coalescence occurring in sequence if the time interval is suitably chosen.
- (3) Bubble breakage is also binary; two and only two daughter bubbles are created from a single bubble per breakage.

3.2 MASTER EQUATION FORMULATION

Figure 3-3 shows the paths of the system entering and leaving its reference state $\{n\}$ at time t in the light of the assumptions made in section 3.1. Performing a probability balance around the reference state gives

(prob. of the system remaining in state $\{n\}$ at time $t+\Delta t$)

$$\begin{aligned}
 = & \left\{ \begin{array}{l} \text{prob. to be in} \\ \text{states } \{n_a\} \\ \text{at time } t \end{array} \right\} \cdot \left\{ \begin{array}{l} \text{corresponding} \\ \text{coalescence} \\ \text{intensities} \end{array} \right\} \cdot \Delta t \\
 & + \left\{ \begin{array}{l} \text{prob. to be in} \\ \text{states } \{n_b\} \\ \text{at time } t \end{array} \right\} \cdot \left\{ \begin{array}{l} \text{corresponding} \\ \text{breakage} \\ \text{intensities} \end{array} \right\} \cdot \Delta t \\
 & + \left\{ \begin{array}{l} \text{prob. to be} \\ \text{in state} \\ \{n\} \text{ at time} \\ t \end{array} \right\} \cdot \left(1 - \left\{ \begin{array}{l} \text{corresponding} \\ \text{coalescence} \\ \text{intensities} \end{array} \right\} \cdot \Delta t - \left\{ \begin{array}{l} \text{corresponding} \\ \text{breakage} \\ \text{intensity} \end{array} \right\} \cdot \Delta t \right)
 \end{aligned} \quad (1)$$

or

$$\begin{aligned}
 P(\{n\}, t+\Delta t) = & \sum_{\{n_a\}} P(\{n_a\}, t) \beta^*(\{n_a\}, \{n\}) \Delta t + \sum_{\{n_b\}} P(\{n_b\}, t) \alpha^*(\{n_b\}, \{n\}) \Delta t \\
 & + P(\{n\}, t) \left[1 - \sum_{\{n_c\}} \beta^*(\{n\}, \{n_c\}) \Delta t \right. \\
 & \left. - \sum_{\{n_d\}} \alpha^*(\{n\}, \{n_d\}) \Delta t \right]
 \end{aligned} \quad (2)$$

where sets $\{n\}$, $\{n_a\}$, $\{n_b\}$, $\{n_c\}$, and $\{n_d\}$ are defined in Fig. 3-3. The intensity functions $\alpha^*(\{*\}, \{*\})$ and $\beta^*(\{*\}, \{*\})$, can be defined through visualization of the following processes based on the binary coalescence and breakage assumptions.

$$(\text{coalescence}) \quad i \in + (j-i) \in \xrightarrow{\beta(i,j)} j \in$$

$$(j/2) \in + (j/2) \in \xrightarrow{\beta(j/2, j/2)} j \in$$

$$\begin{aligned}
 (\text{breakage}) \quad j \in \frac{\alpha(j,i)}{\Omega} (j-i)\epsilon + i\epsilon \\
 j \in \frac{\alpha(j,j/2)}{\Omega} (j/2)\epsilon + (j/2)\epsilon
 \end{aligned}$$

These mechanisms lead to

$$\begin{aligned}
 \beta^*(\{*\}, \{*\}) &= dn_j/dt = \begin{cases} \frac{\beta(i,j)}{\Omega} n_i n_{j-i}; & i \neq j/2, i < j \\ \frac{\beta(i,j)}{\Omega} n_{j/2} (n_{j/2} - 1); & i = j/2 \end{cases} \\
 \alpha^*(\{*\}, \{*\}) &= -dn_j/dt = \alpha(j,i) n_j; \quad i < j
 \end{aligned} \quad (3)$$

Applying the definitions of the intensity functions into eqn. (2), explicitly specifying the upper and lower bounds of the resultant equation after taking the limits of $\Delta t \rightarrow 0$ yields the probability balance equation for the system,

$$\begin{aligned}
 \frac{\partial P(\{n\}, t)}{\partial t} &= \sum_{j=3}^{\infty} \sum_{i=1}^{\lfloor \frac{j-1}{2} \rfloor} \frac{\beta(i,j)}{\Omega} (n_i + 1) (n_{j-i} + 1) P(\{n_{a1}\}, t) \\
 &+ \sum_{\substack{j=2 \\ \text{even}}}^{\infty} \frac{\beta(j/2, j)}{\Omega} (n_{j/2} + 2) (n_{j/2} + 1) P(\{n_{a2}\}, t) \\
 &+ \sum_{j=3}^{\infty} \sum_{i=1}^{\lfloor \frac{j-1}{2} \rfloor} \alpha(j, i) (n_j + 1) P(\{n_{b1}\}, t) \\
 &+ \sum_{\substack{j=2 \\ \text{even}}}^{\infty} \alpha(j, j/2) (n_j + 1) P(\{n_{b2}\}, t) \\
 &- \sum_{j=3}^{\infty} \sum_{i=1}^{\lfloor \frac{j-1}{2} \rfloor} \left[\frac{\beta(i,j)}{\Omega} n_i n_{j-i} + \alpha(j, i) n_j \right] P(\{n\}, t) \quad (4)
 \end{aligned}$$

An equation involving incremental changes, e.g., eqn. (4), can be written in a more compact form by introducing the "step operator" advocated by van Kampen. The step operator, E_a^b , is so defined that the subscript, a , denotes the position while the superscript, b , denotes the step size of the incremental change. For example,

$$E_a^b(x_a + x_c) = (x_a + b) + x_c \quad (5)$$

Thus,

$$E_i^1 E_{j-i}^1 E_j^{-1} n_i n_{j-i} P(\{n\}, t) = (n_i + 1)(n_{j-i} + 1) P(\{n'\}, t) \quad (6)$$

where

$$\{n\} = \{n_1, n_2, \dots, n_i, \dots, n_{j-1}, \dots, n_j, \dots\}$$

$$\{n'\} = \{n_1, n_2, \dots, n_i + 1, \dots, n_{j-i} + 1, \dots, n_j - 1, \dots\}$$

By resorting to the step operators, the master equation, eqn. (4), can be rewritten as

$$\begin{aligned} \dot{P}(\{n\}, t) = & \sum_{j=3}^{\infty} \sum_{i=1}^{\lfloor \frac{j-1}{2} \rfloor} \left[\frac{\beta(i, j)}{\Omega} (E_i^1 E_{j-i}^1 E_j^{-1} - 1) n_i n_{j-i} P(\{n\}, t) \right] \\ & + \sum_{\substack{j=2 \\ \text{even}}}^{\infty} \left[\frac{\beta(j/2, j)}{\Omega} (E_{j/2}^2 E_j^{-1} - 1) n_{j/2} (n_{j/2} - 1) P(\{n\}, t) \right] \\ & + \sum_{j=3}^{\infty} \sum_{i=1}^{\lfloor \frac{j-1}{2} \rfloor} \{ \alpha(j, i) (E_i^{-1} E_{j-i}^{-1} E_j^1 - 1) n_j P(\{n\}, t) \} \\ & + \sum_{\substack{j=2 \\ \text{even}}}^{\infty} \{ \alpha(j, j/2) (E_{j/2}^{-2} E_j^1 - 1) n_j P(\{n\}, t) \} \quad (7) \end{aligned}$$

$$\begin{aligned}
\dot{P} = & \sum_{j=3}^{\infty} \sum_{i=1}^{\lfloor \frac{j-1}{2} \rfloor} \left\{ \frac{\beta(i,j)}{\Omega} (E_1^1 E_{j-1}^1 E_j^{-1} - 1) n_i n_{j-1} P \right\} \\
& + \sum_{j=1}^{\infty} \left\{ \frac{\beta(j,2j)}{\Omega} (E_j^2 E_{2j}^{-1} - 1) n_j (n_j - 1) P \right\} \\
& + \sum_{j=3}^{\infty} \sum_{i=1}^{\lfloor \frac{j-1}{2} \rfloor} \left\{ \alpha(j,i) (E_i^{-1} E_{j-1}^{-1} E_j^1 - 1) n_j P \right\} \\
& + \sum_{j=1}^{\infty} \left\{ \alpha(2j,j) (E_j^{-2} E_{2j}^1 - 1) n_{2j} P \right\} \quad (8)
\end{aligned}$$

In spite of its obvious physical significance, only in rare cases can the nonlinear master equation*, eqn. (8), be solved explicitly. A systematic means for resolving this difficulty is the master equation expansion. The technique is developed in the form of a power series expansion in a parameter Ω . Accordingly, we shall first transform eqn. (8) into an approximate continuous form. To accomplish this, we replace the discrete variable set $\{n\}$ with a continuous function $n(V)$ as illustrated in Fig. 3-4. The step operator and its effect on a continuous function $n(V)$ are now defined as

$$E_a^b n(V) = n(V) + bI(V-a) \quad (9)$$

where $I(V-a)$ is an index function defined as

* The non-linearity of the master equation is perceived in terms of its coefficients.

$$\begin{aligned}
 I(V-a) &= 1 && @ V = a \\
 &= 0 && \text{elsewhere}
 \end{aligned}$$

Also, in reference to Fig. 3-4, we can write

$$\begin{aligned}
 n_1 &= n\left(\frac{1}{2}\epsilon\right) \\
 n_2 &= n\left(\frac{3}{2}\epsilon\right) \\
 &\vdots \\
 n_i &= n\left(\frac{2i-1}{2}\epsilon\right) = n(v) \\
 &\vdots \\
 n_j &= n\left(\frac{2j-1}{2}\epsilon\right) = n(v')
 \end{aligned} \tag{10}$$

and

$$\begin{aligned}
 \alpha(j, i) &= \alpha\left(\frac{2j-1}{2}\epsilon, \frac{2i-1}{2}\epsilon\right) = \alpha(v', v) \\
 \beta(i, j) &= \beta\left(\frac{2i-1}{2}\epsilon, \frac{2j-1}{2}\epsilon\right) = \beta(v, v')
 \end{aligned} \tag{11}$$

The master equation expressed in continuous form is then (see APPENDIX

A)

$$\begin{aligned}
 \dot{P}(n(V), t) &= \lim_{\epsilon \rightarrow 0} \frac{1}{\epsilon} \left\{ \int_0^{\frac{v'}{2}} \int_0^{\frac{v'}{2}} a(v', v) \left[E_v^{-1} E_{v'-v}^{-1} E_v^1, -1 \right] n(v') P dv dv' \right. \\
 &\quad + \int_0^\infty \int_0^\infty a^*(\omega, v) I(\omega=2v) \left[E_v^{-2} E_\omega^1 - 1 \right] n(\omega) P dv d\omega \\
 &\quad \left. + \int_0^{\frac{v'}{2}} \int_0^{\frac{v'}{2}} \frac{b(v, v')}{\Omega} \left[E_v^1 E_{v'-v}^1 E_{v'}^{-1}, -1 \right] n(v) n(v'-v) P dv dv' \right\}
 \end{aligned}$$

$$+ \int_0^\infty \int_0^\infty \frac{b^*(v, \omega)}{\Omega} I(\omega - 2v) \left[E_v^2 E_\omega^{-1} - 1 \right] n(v) [n(v) - 1] P dv d\omega \quad (12)$$

The presence of step operators in eqn. (12) renders its mathematical manipulation unwieldy. This can be circumvented through clarification of the relationship between the step operator and Taylor series expansion. A Taylor series expansion applied to an arbitrary function $f(x)$ yields

$$f(x+\Delta x) - f(x) = \frac{\partial f}{\partial x}(\Delta x) + \frac{1}{2!} \frac{\partial^2 f}{\partial x^2}(\Delta x)^2 + \dots \quad (13)$$

Here, the function of interest is $p(n, t)$. Expanding it with respect to n yields

$$p(n+\Delta n, t) - p(n, t) = \frac{\partial p}{\partial n}(\Delta n) + \frac{1}{2!} \frac{\partial^2 p}{\partial n^2}(\Delta n)^2 + \dots \quad (14)$$

where Δn can be chosen to be $bI(V-a)$; by definition [see eqn. (9)]

$$(E_a^b - 1)p(n, t) = b \left. \frac{\partial p}{\partial n} \right|_{V=a} + \frac{b^2}{2!} \left. \frac{\partial^2 p}{\partial n^2} \right|_{V=a} + \dots \quad (15)$$

By operating both sides of eqn. (15) through a second step operator, we obtain

$$E_c^d (E_a^b - 1)p(n, t) = E_c^d \left(b \left. \frac{\partial p}{\partial n} \right|_{V=a} + \frac{b^2}{2!} \left. \frac{\partial^2 p}{\partial n^2} \right|_{V=a} + \dots \right) \quad (16)$$

The step operator has no effect on the right hand side of this equation because all terms inside the parentheses are constants; thus,

$$\begin{aligned} E_c^d E_a^b p(n, t) &= [p(n, t) + d \left. \frac{\partial p}{\partial n} \right|_{V=c} + \frac{d^2}{2!} \left. \frac{\partial^2 p}{\partial n^2} \right|_{V=c} + \dots] \\ &= b \left. \frac{\partial p}{\partial n} \right|_{V=a} + \frac{b^2}{2!} \left. \frac{\partial^2 p}{\partial n^2} \right|_{V=a} + \dots \end{aligned} \quad (17)$$

or equivalently,

$$\begin{aligned}
(E_c^d E_a^b - 1)p(n, t) = & b \frac{\partial p}{\partial n} \bigg|_{V=a} + \frac{b^2}{2!} \frac{\partial^2 p}{\partial n^2} \bigg|_{V=a} + \dots \\
& + d \frac{\partial p}{\partial n} \bigg|_{V=c} + \frac{d^2}{2!} \frac{\partial^2 p}{\partial n^2} \bigg|_{V=c} + \dots
\end{aligned} \quad (18)$$

Repeating the procedure gives

$$\begin{aligned}
(E_a^b E_c^d E_e^f - 1) = & b \frac{\partial}{\partial n} \bigg|_{V=a} + \frac{b^2}{2!} \frac{\partial^2}{\partial n^2} \bigg|_{V=a} + \dots \\
& + d \frac{\partial}{\partial n} \bigg|_{V=c} + \frac{d^2}{2!} \frac{\partial^2}{\partial n^2} \bigg|_{V=c} + \dots \\
& + f \frac{\partial}{\partial n} \bigg|_{V=e} + \frac{f^2}{2!} \frac{\partial^2}{\partial n^2} \bigg|_{V=e} + \dots
\end{aligned} \quad (19)$$

3.3 MASTER EQUATION EXPANSION

Due to the law of large numbers, we can expect that the probability of a random variable, e.g., $n(V)$, to have a distribution with a sharp maximum around its macroscopic value, denoted here as $n = \Omega \phi$, and a width of order $\Omega^{1/2} \phi^{1/2}$. Therefore, we can write

$$n(V, t) = \Omega \phi(V, t) + \Omega^{1/2} x(V, t) \quad (20)$$

This equation is the basis of the so-called master equation expansion in which a random variable is expressed as a linear combination of two parts, namely, a deterministic component and a stochastic component. The expansion parameter Ω governs the extent of fluctuations. Often, Ω can simply be the size of the system. Also in eqn. (20), ϕ is the deterministic solution while x is a new random variable replacing n . Accordingly,

the probability distribution function $p(n,t)$ can be rewritten as a function of x as

$$p(n,t)dn = \pi(x,t)dx \quad (21)$$

Equations (20) and (21) lead to a sequence of transform functions

$$\partial n = \Omega^{1/2} \partial x \quad (22)$$

$$\frac{\partial \pi}{\partial x} = \frac{\partial p}{\partial n} \left(\frac{\partial n}{\partial x} \right)^2 = \Omega \frac{\partial p}{\partial n} \quad (23)$$

$$\begin{aligned} \frac{\partial \pi}{\partial t} &= \frac{\partial n}{\partial x} \frac{\partial p}{\partial t} + \frac{\partial n}{\partial x} \frac{\partial p}{\partial n} \frac{\partial n}{\partial t} \\ &= \Omega^{1/2} \frac{\partial p}{\partial t} + \left(\Omega^{-1/2} \frac{\partial \pi}{\partial x} \right) \left(\Omega \frac{\partial \theta}{\partial t} \right) \end{aligned} \quad (24)$$

From eqns. (19) and (22), we have

$$\begin{aligned} (E_a^b E_c^d E_e^f - 1) &\approx b \Omega^{-1/2} \left. \frac{\partial}{\partial x} \right|_{V=a} + \frac{b^2}{2!} \Omega^{-1} \left. \frac{\partial^2}{\partial x^2} \right|_{V=a} \\ &\quad + d \Omega^{-1/2} \left. \frac{\partial}{\partial x} \right|_{V=c} + \frac{d^2}{2!} \Omega^{-1} \left. \frac{\partial^2}{\partial x^2} \right|_{V=c} \\ &\quad + f \Omega^{-1/2} \left. \frac{\partial}{\partial x} \right|_{V=e} + \frac{f^2}{2!} \Omega^{-1} \left. \frac{\partial^2}{\partial x^2} \right|_{V=e} \end{aligned} \quad (26)$$

Note that eqn. (26) is essentially eqn. (19) written in terms of Ω with higher order terms from the Taylor series expansion truncated. The truncation will not cause any significant error if the parameter is suitably chosen. Substituting eqns. (20), (25), and (26) into the master equation, eqn. (12), yields

$$\begin{aligned}
& \Omega^0 \frac{\partial \pi}{\partial t} - \Omega^{\frac{1}{2}} \frac{\partial \phi}{\partial t} \frac{\partial \pi}{\partial x} \\
& = \lim_{\varepsilon \rightarrow 0} \frac{1}{\varepsilon} \left\{ \int_0^\infty \int_0^{\frac{v'}{2}} a(v', v) \left[-\Omega^{-\frac{1}{2}} \frac{\partial}{\partial x} \bigg|_{v=v} - \Omega^{-\frac{1}{2}} \frac{\partial}{\partial x} \bigg|_{v=v'-v} + \Omega^{-\frac{1}{2}} \frac{\partial}{\partial x} \bigg|_{v=v'} \right. \right. \\
& \quad \left. \left. + \frac{1}{2} \Omega^{-1} \frac{\partial^2}{\partial x^2} \bigg|_{v=v} + \frac{1}{2} \Omega^{-1} \frac{\partial^2}{\partial x^2} \bigg|_{v=v'-v} + \frac{1}{2} \Omega^{-1} \frac{\partial^2}{\partial x^2} \bigg|_{v=v'} \right] \right. \\
& \quad \left. \cdot (\Omega \phi(v') + \Omega^{\frac{1}{2}} x(v')) \pi dv dv' \right. \\
& \quad + \int_0^\infty \int_0^\infty a^*(\omega, v) I(\omega - 2v) \left[-2\Omega^{-\frac{1}{2}} \frac{\partial}{\partial x} \bigg|_{v=v} + \Omega^{-\frac{1}{2}} \frac{\partial}{\partial x} \bigg|_{v=\omega} \right. \\
& \quad \left. + \frac{4}{2} \Omega^{-1} \frac{\partial^2}{\partial x^2} \bigg|_{v=v} + \frac{1}{2} \Omega^{-1} \frac{\partial^2}{\partial x^2} \bigg|_{v=\omega} \right] \\
& \quad \left. \cdot (\Omega \phi(\omega) + \Omega^{\frac{1}{2}} x(\omega)) \pi dv d\omega \right. \\
& \quad + \int_0^\infty \int_0^{\frac{v'}{2}} \frac{b(v, v')}{\Omega} \left[\Omega^{-\frac{1}{2}} \frac{\partial}{\partial x} \bigg|_{v=v} + \Omega^{-\frac{1}{2}} \frac{\partial}{\partial x} \bigg|_{v=v'-v} - \Omega^{-\frac{1}{2}} \frac{\partial}{\partial x} \bigg|_{v=v'} \right. \\
& \quad \left. + \frac{1}{2} \Omega^{-1} \frac{\partial^2}{\partial x^2} \bigg|_{v=v} + \frac{1}{2} \Omega^{-1} \frac{\partial^2}{\partial x^2} \bigg|_{v=v'-v} + \frac{1}{2} \Omega^{-1} \frac{\partial^2}{\partial x^2} \bigg|_{v=v'} \right] \\
& \quad \left. \cdot (\Omega \phi(v) + \Omega^{\frac{1}{2}} x(v)) (\Omega \phi(v'-v) + \Omega^{\frac{1}{2}} x(v'-v)) \pi dv dv' \right. \\
& \quad + \int_0^\infty \int_0^\infty \frac{b^*(v, \omega)}{\Omega} I(\omega - 2v) \left[2\Omega^{-\frac{1}{2}} \frac{\partial}{\partial x} \bigg|_{v=v} - \Omega^{-\frac{1}{2}} \frac{\partial}{\partial x} \bigg|_{v=\omega} \right. \\
& \quad \left. + \frac{4}{2} \Omega^{-1} \frac{\partial^2}{\partial x^2} \bigg|_{v=v} + \frac{1}{2} \Omega^{-1} \frac{\partial^2}{\partial x^2} \bigg|_{v=\omega} \right] (\Omega \phi(v) + \Omega^{\frac{1}{2}} x(v)) \\
& \quad \left. \cdot (\Omega \phi(v) + \Omega^{\frac{1}{2}} x(v) - 1) \pi dv d\omega \right\} \quad (27)
\end{aligned}$$

Collecting terms of order $\Omega^{1/2}$ in eqn. (27) gives rise to the following macroscopic equation for the system;

$$\begin{aligned}
 & -\frac{\partial \phi}{\partial t} \frac{\partial \pi}{\partial x} \\
 = & \lim_{\varepsilon \rightarrow 0} \frac{1}{\varepsilon} \left\{ \int_0^\infty \int_0^\infty \frac{v'}{2} a(v', v) \left[-\frac{\partial}{\partial x} \right]_{v=v} - \frac{\partial}{\partial x} \right]_{v=v'-v} + \frac{\partial}{\partial x} \left[\phi(v') \pi dv dv' \right. \right. \\
 & + \int_0^\infty \int_0^\infty a^*(\omega, v) I(\omega-2v) \left[-2 \frac{\partial}{\partial x} \right]_{v=v} + \frac{\partial}{\partial x} \left[\phi(\omega) \pi dv d\omega \right. \\
 & + \int_0^\infty \int_0^\infty \frac{v'}{2} b(v, v') \left(\frac{\partial}{\partial x} \right)_{v=v} + \frac{\partial}{\partial x} \left[\phi(v) \phi(v'-v) \pi dv dv' \right. \\
 & \left. \left. + \int_0^\infty \int_0^\infty b^*(v, \omega) I(\omega-2v) \left(2 \frac{\partial}{\partial x} \right)_{v=v} - \frac{\partial}{\partial x} \left[\phi(v) \phi(v) \pi dv d\omega \right] \right] \right\} \quad (28)
 \end{aligned}$$

Collecting terms of order Ω^0 from eqn. (27) yields the Fokker-Planck equation of the system given below -

$$\begin{aligned}
 \frac{\partial \pi}{\partial t} = & \lim_{\varepsilon \rightarrow 0} \frac{1}{\varepsilon} \left\{ \int_0^\infty \int_0^\infty \frac{v'}{2} a(v', v) \left[\left(-\frac{\partial}{\partial x} \right)_{v=v} - \frac{\partial}{\partial x} \right]_{v=v'-v} + \frac{\partial}{\partial x} \left[\phi(v') \pi(v') \right. \right. \\
 & \left. \left. + \frac{1}{2} \left(\frac{\partial^2}{\partial x^2} \right)_{v=v} + \frac{\partial^2}{\partial x^2} \right]_{v=v'-v} + \frac{\partial^2}{\partial x^2} \left[\phi(v') \right] \pi dv dv' \right. \\
 & + \int_0^\infty \int_0^\infty a^*(\omega, v) I(\omega-2v) \left[\left(-2 \frac{\partial}{\partial x} \right)_{v=v} + \frac{\partial}{\partial x} \right]_{v=\omega} \pi(\omega) \\
 & \left. + \frac{1}{2} \left(4 \frac{\partial^2}{\partial x^2} \right)_{v=v} + \frac{\partial^2}{\partial x^2} \right]_{v=\omega} \phi(\omega) \pi dv d\omega \right. \\
 & \left. + \int_0^\infty \int_0^\infty \frac{v'}{2} b(v, v') \left(\frac{\partial}{\partial x} \right)_{v=v} + \frac{\partial}{\partial x} \left[\phi(v) \phi(v'-v) \right] \pi dv dv' \right\}
 \end{aligned}$$

$$\begin{aligned}
& (\phi(v)x(v'-v) + \phi(v'-v)x(v)) + \frac{1}{2} \left(\frac{\partial^2}{\partial x^2} \right)_{V=v} + \frac{\partial^2}{\partial x^2} \Big|_{V=v'-v} \\
& + \frac{\partial^2}{\partial x^2} \Big|_{V=v'}) \phi(v) \phi(v'-v)] \pi dv dv' \\
& + \left\{ \int_0^\infty \int_0^\infty b^*(v, \omega) I(\omega - 2v) \left[\left(2 \frac{\partial}{\partial x} \right)_{V=v} - \frac{\partial}{\partial x} \Big|_{V=\omega} \right] \right. \\
& \left. (2\phi(v)x(v)) + \frac{1}{2} \left(4 \frac{\partial^2}{\partial x^2} \Big|_{V=v} + \frac{\partial^2}{\partial x^2} \Big|_{V=\omega} \right) \phi^2(v) \right] \pi dv d\omega \right\} \\
& \quad (29)
\end{aligned}$$

Carefully rearranging eqn. (28) leads to a compact form (see Appendix B)

$$\begin{aligned}
\frac{\partial \phi(V)}{\partial t} &= \int_0^\infty a'(v, V) \phi(v) dv \\
&- \frac{1}{2} \int_0^V a'(V, v) \phi(V) dv \\
&+ \int_0^V b'(v, V) \phi(v) \phi(V-v) dv \\
&- \int_0^\infty b'(V, V+v) \phi(V) \phi(v) dv \quad (30)
\end{aligned}$$

The term on the left-hand side of the above equation denotes the rate of change of the bubble density (for bubbles of size V). On the right hand side of the equation, the first two terms represent the bubble density increase and decrease, respectively, due to bubble breakage while the last two terms those due to bubble coalescence. Equation (30) holds for every possible bubble size V . Thus, the resultant set of equations can be used to solve for a bubble size distribution in the system at any instance.

Equally important is the information that can be retrieved from the Fokker-Planck equation, eqn. (27). By applying an approach similar to that employed in deriving eqn. (30) from eqn. (29), we can recover any moment of the random variable x . For instance, the first and the second moments of x are, respectively (see Appendix C),

$$\begin{aligned} \frac{d\langle x(V) \rangle}{dt} = & \int_V^\infty a'(v, V) \langle x(v) \rangle dv \\ & - \frac{1}{2} \int_0^V a'(V, v) \langle x(V) \rangle dv \\ & + \int_0^{\frac{V}{2}} b'(v, V) [\phi(v) \langle x(V-v) \rangle + \phi(V-v) \langle x(v) \rangle] dv \\ & - \int_0^\infty b'(V, V+v) [\phi(V) \langle x(v) \rangle + \phi(v) \langle x(V) \rangle] dv \end{aligned} \quad (31)$$

$$\begin{aligned} \frac{d\langle x(V)^2 \rangle}{dt} = & 2 \int_V^\infty a'(v, V) \langle x(v)^2 \rangle dv \\ & - \int_0^V a'(V, v) \langle x(V)^2 \rangle dv \\ & + 2 \int_0^{\frac{V}{2}} b'(v, V) [\phi(v) \langle x(V-v)^2 \rangle + \phi(V-v) \langle x(v)^2 \rangle] dv \\ & - 2 \int_0^\infty b'(V, V+v) [\phi(V) \langle x(v)^2 \rangle + \phi(v) \langle x(V)^2 \rangle] dv \\ & + \int_V^\infty a'(v, V) \phi(v) dv \\ & + \frac{1}{2} \int_0^V a'(V, v) \phi(V) dv \\ & + \int_0^{\frac{V}{2}} b'(v, V) \phi(v) \phi(V-v) dv \\ & + \int_0^\infty b'(V, V+v) \phi(V) \phi(v) dv \end{aligned} \quad (32)$$

3.4 EXTENSION TO AN OPEN SYSTEM

The master equation model established in the previous sections is for the closed system. Nevertheless, it can be extended to an open system simply by including terms for input and output in the right-hand side of eqn. (12). An example of such a system is a fluidized bed where bubbles are generated from the gas distributor at the bottom and disappear from the top. The input term is

$$I_n = \int_0^{\infty} \Omega \zeta(v) P(n(v) - I(V-v), t) dv - \int_0^{\infty} \Omega \zeta(v) P(n(V), t) dv \quad (33a)$$

or

$$I_n = \int_0^{\infty} \Omega \zeta(v) (E_v^{-1} - 1) P(n(V), t) dv \quad (33b)$$

and the output term is

$$O_n = \int_0^{\infty} \zeta(v) P(n(V) + I(V-v), t) dv - \int_0^{\infty} \Omega \zeta(n(V), t) dv \quad (34a)$$

or

$$O_n = \int_0^{\infty} \zeta(v) (E_v^1 - 1) n(v) P(n(V), t) dv \quad (34b)$$

where $\Omega \zeta(v) dv$ is the rate at which the bubbles of sizes ranging from v to $v+dv$ enter the system, and $\zeta(v) dv$ is the rate at which the bubbles of sizes ranging from v to $v+dv$ leave the system. Thus, the first term in eqn. (33a) is the rate of change of the probability for the system to reach a reference state $n(V)$, while the second term that for it to leave a reference state. The terms in eqn. (34a) can be interpreted similarly.

Note that eqn. (33a) or (33b) does not explicitly contain the random variable, $n(V)$, because the mode of bubble generation at the distributor

is specified in the present modeling without regard to the bubble coalescence and breakage governing the system behavior. Also note that Ω appears explicitly in this equation, and thus the input term represented by the equation contributes to the population balance equation resulting from the master equation expansion.

3.5 A CASE STUDY: TWO-BUBBLE-SIZE SYSTEM

A simple two-phase closed system, consisting of an emulsion phase and a bubble phase, which is restricted to having only two different bubble sizes, is employed to illustrate the master equation expansion technique. An example of a two-bubble-size system can be a fluidized bed or a bubble column under certain condition. The case study can be initiated by writing the system volume conservation equation for the bubble phase, namely,

$$V = n_1 V_1 + n_2 V_2 \quad (35a)$$

From eqn. (20), we obtain

$$V = (\emptyset_1 \Omega + x_1 \Omega^{\frac{1}{2}}) V_1 + (\emptyset_2 \Omega + x_2 \Omega^{\frac{1}{2}}) V_2 \quad (35b)$$

where V is the total volume of the bubble phase, Ω the total volume of the system, n_1 the number of smaller bubbles of volume V_1 , and n_2 that of larger bubbles of volume V_2 . Since the system is of two bubble sizes, it is obvious that $V_2 = 2V_1$. Let a_{21} be the bubble breakage rate and b_{12} the coalescence rate. Hence, at any time instance,

$$\begin{aligned} N_1 &= V/V_1 \\ &= n_1(t) + 2n_2(t) \\ &= (\emptyset_1(t) + 2\emptyset_2(t))\Omega + (x_1(t) + 2x_2(t))\Omega^{\frac{1}{2}} \end{aligned} \quad (36)$$

In what follows, time t will be eliminated for simplicity; in other words, n_1 , n_2 , θ_1 , θ_2 , x_1 , and x_2 are all understood to be functions of time.

Master equation expansion gives rise to the following sequence of equations, corresponding to the sequence of equations, eqns. (30) to (32).

(i) Population balance equations:

$$\frac{d\theta_1}{dt} = a_{21}\theta_2 - b_{12}\theta_1^2 \quad (37a)$$

$$\frac{d\theta_2}{dt} = -\frac{1}{2} a_{21}\theta_2 + \frac{1}{2} b_{12}\theta_1^2 \quad (37b)$$

(ii) first moment equations:

$$\frac{d\langle x_1 \rangle}{dt} = a_{21}\langle x_2 \rangle - b_{12}\theta_1\langle x_1 \rangle \quad (38a)$$

$$\frac{d\langle x_2 \rangle}{dt} = -\frac{1}{2} a_{21}\langle x_2 \rangle + \frac{1}{2} b_{12}\theta_1\langle x_1 \rangle \quad (38b)$$

(iii) second moment equations:

$$\frac{d\langle x_1^2 \rangle}{dt} = 2a_{21}\langle x_1^2 \rangle - 4b_{12}\theta_1\langle x_1^2 \rangle + a_{21}\theta_2 + b_{12}\theta_1^2 \quad (39)$$

$$\frac{d\langle x_2^2 \rangle}{dt} = -\frac{1}{2} a_{21}\langle x_2^2 \rangle + b_{12}\theta_1\langle x_1^2 \rangle + \frac{1}{2} a_{21}\theta_2 + \frac{1}{2} b_{12}\theta_1^2 \quad (40)$$

Of these seven equations, six are independent, from which six unknowns, θ_1 , θ_2 , $\langle x_1 \rangle$, $\langle x_2 \rangle$, $\langle x_1^2 \rangle$, and $\langle x_2^2 \rangle$ can be determined.

First, the sum of eqn. (37a) and twice of eqn. (37b) gives

$$\frac{d(\theta_1 + 2\theta_2)}{dt} = 0 \quad (41)$$

from which we conclude that

$$\phi_1 + 2\phi_2$$

is constant. In other words, we can write

$$\phi_1 + 2\phi_2 = \phi_1(0) + 2\phi_2(0) \quad (42)$$

The equality must hold under any circumstances, even when

$$\phi_2(0) = 0$$

Thus,

$$\phi_1(0) + 2\phi_2(0) = \phi_1(0) = \frac{V}{V_1\Omega} \quad (43)$$

and

$$\phi_1 + 2\phi_2 = \frac{V}{V_1\Omega} = \frac{N_1}{\Omega} \quad (44)$$

This implies that ϕ_2 can be expressed in terms of ϕ_1 or vice versa.

Consequently, from eqns. (37a) and (44), we obtain

$$\frac{d\phi_1}{dt} = \frac{a_{21}}{2} \left(\frac{N_1}{\Omega} - \phi_1 \right) - b_{12}\phi_1^2 \quad (45)$$

This is a nonlinear first order O.D.E.; its solution is (see Appendix D),

$$\phi_1 = (A + B) \frac{1 - \frac{\phi_1(0) - (A+B)}{\phi_1(0) - (A+B)} \frac{A-B}{A+B} e^{-2Bb_{12}t}}{1 - \frac{\phi_1(0) - (A+B)}{\phi_1(0) - (A-B)} e^{-2Bb_{12}t}} \quad (46)$$

and, thus, we find from eqn. (44)

$$\phi_2 = \frac{1}{2} \left(\frac{N_1}{\Omega} - \phi_1 \right) \quad (47)$$

where

$$A = -\frac{a_{21}}{4b_{12}} \quad (48)$$

$$B = \frac{1}{2} \sqrt{\left(\frac{a_{21}}{2b_{12}}\right)^2 + \frac{2a_{21}N_1}{b_{12}\Omega}} \quad (49)$$

Taking the limits as $t \rightarrow \infty$, we find ϕ_1 converging to a constant value of $(A+B)$, which is the steady state solution ϕ_{1s} given as (see Appendix E)

$$\phi_{1s} = A+B = \frac{-a_{21}\Omega + \sqrt{a_{21}^2\Omega^2 + 8a_{21}b_{12}N_1\Omega}}{4b_{12}\Omega} \quad (50)$$

This together with eqn. (37a) yield (also see Appendix E)

$$\phi_{2s} = \frac{b_{12}}{a_{21}} \phi_{1s}^2 \quad (51)$$

Equations (46) and (47) are the transient solutions for the macroscopic bubble densities. Next, we shall examine the stochastic behavior of the system under a macroscopically steady-state condition. To do so, a small perturbation, of order $\phi^{1/2}$, of the fluctuating component, x , will be imposed on the system, and the subsequent behavior of the first and second moments of the fluctuating component will be studied. The solution for the first moment of the random variable, x , is again initiated by summing eqn. (38a) and two times eqn. (28b), obtaining

$$\frac{d(\langle x_1 \rangle + 2\langle x_2 \rangle)}{dt} = 0 \quad (52)$$

This results in

$$\langle x_1 \rangle + 2 \langle x_2 \rangle = \langle x_1(0) \rangle + 2 \langle x_2(0) \rangle \quad (53)$$

By resorting to the macroscopic steady-state version of eqn. (20), i.e.,

$$n(t) = \phi_{1s} \Omega + x(t) \Omega^{\frac{1}{2}} \quad (54)$$

we obtain the initial conditions

$$\langle x_1(0) \rangle = \frac{n_1(0) - \phi_{1s} \Omega}{\Omega^{\frac{1}{2}}} \quad (55)$$

$$\langle x_2(0) \rangle = \frac{\phi_{1s} \Omega - n_1(0)}{2\Omega^{\frac{1}{2}}} \quad (56)$$

$n_1(0)$ and $n_2(0)$ in these expressions are always integers while $\langle x_1(0) \rangle$, $\langle x_2(0) \rangle$, and ϕ_{1s} are real numbers. $\langle x_1(0) \rangle$ and $\langle x_2(0) \rangle$ generally are not zero. Combining eqns. (38a) and (53) yields

$$\frac{\langle x_1 \rangle}{\langle x_1(0) \rangle} = \frac{\int \frac{d\langle x_1 \rangle}{\langle x_1 \rangle - \frac{a_{21}(\langle x_1(0) \rangle + 2\langle x_2(0) \rangle)}{a_{21} + 2b_{12}\phi_{1s}}} = -\int_0^t \left(\frac{a_{21}}{2} + b_{12}\phi_{1s} \right) dt \quad (57)$$

Thus,

$$\frac{(a_{21} + 2b_{12}\phi_{1s})\langle x_1 \rangle - a_{21}(\langle x_1(0) \rangle + 2\langle x_2(0) \rangle)}{2b_{12}\phi_{1s}\langle x_1(0) \rangle - 2\langle x_2(0) \rangle} = \exp \left[\left(-\frac{a_{21} + 2b_{12}\phi_{1s}}{2} \right) t \right] \quad (58)$$

or

$$\begin{aligned} \langle x_1 \rangle = & \frac{2b_{12}\phi_{1s}\langle x_1(0) \rangle - 2\langle x_2(0) \rangle}{a_{21} + 2b_{12}\phi_{1s}} \exp \left[\left(-\frac{a_{21} + 2b_{12}\phi_{1s}}{2} \right) t \right] \\ & + \frac{a_{21}(\langle x_1(0) \rangle + 2\langle x_2(0) \rangle)}{a_{21} + 2b_{12}\phi_{1s}} \end{aligned} \quad (59)$$

from which $\langle x_2 \rangle$ is solved to be

$$\begin{aligned} \langle x_2 \rangle = & - \frac{b_{12} \theta_{1s} \langle x_1(0) \rangle - \langle x_2(0) \rangle}{a_{21} + 2b_{12} \theta_{1s}} \exp \left[\left(- \frac{a_{21} + 2b_{12} \theta_{1s}}{2} \right) t \right] \\ & + \frac{b_{12} \theta_{1s} (\langle x_1(0) \rangle + 2 \langle x_2(0) \rangle)}{a_{21} + 2b_{12} \theta_{1s}} \end{aligned} \quad (60)$$

The boundary conditions require that as $t \rightarrow \infty$

$$\langle x_1(\infty) \rangle = \langle x_2(\infty) \rangle = 0 \quad (61)$$

from which we can show that

$$\langle x_1 \rangle + 2 \langle x_2 \rangle = \langle x_1(0) \rangle + 2 \langle x_2(0) \rangle = 0 \quad (62)$$

Hence,

$$\langle x_1 \rangle = \frac{2b_{12} \theta_{1s} \langle x_1(0) \rangle - 2 \langle x_2(0) \rangle}{a_{21} + 2b_{12} \theta_{1s}} \exp \left[\left(- \frac{a_{21} + 2b_{12} \theta_{1s}}{2} \right) t \right] \quad (63)$$

$$\langle x_2 \rangle = - \frac{b_{12} \theta_{1s} \langle x_1(0) \rangle - \langle x_2(0) \rangle}{a_{21} + 2b_{12} \theta_{1s}} \exp \left[\left(- \frac{a_{21} + 2b_{12} \theta_{1s}}{2} \right) t \right] \quad (64)$$

These results show that the means of the random fluctuations will converge exponentially to zero as time proceeds.

Furthermore, the second moments of the random variables $\langle x_1^2 \rangle$ and $\langle x_2^2 \rangle$ can be solved from eqns. (39) and (40) for the macroscopic steady state. Taking the second derivatives of eqns. (39) and (40) gives rise to

$$\frac{d^2 \langle x_1^2 \rangle}{dt^2} = 2a_{21} \frac{d \langle x_2^2 \rangle}{dt} - 4b_{12} \theta_{1s} \frac{d \langle x_1^2 \rangle}{dt} \quad (65)$$

$$\frac{d^2 \langle x_2^2 \rangle}{dt^2} = - \frac{1}{2} a_{21} \frac{d \langle x_2^2 \rangle}{dt} + b_{12} \theta_{1s} \frac{d \langle x_1^2 \rangle}{dt} \quad (66)$$

Summing the results gives

3-23

$$\frac{d^2(\langle x_1^2 \rangle + 4\langle x_2^2 \rangle)}{dt} = 0 \quad (67)$$

or equivalently,

$$\langle x_1^2 \rangle + 4\langle x_2^2 \rangle = c_1 t + c_2 \quad (68)$$

From the equation above, $\langle x_2^2 \rangle$ can be expressed in terms of $\langle x_1^2 \rangle$.

Substituting the resultant relationship into eqn. (65) yields,

$$\frac{d^2 \langle x_1^2 \rangle}{dt^2} = 2a_{21} \left(\frac{c_1}{4} - \frac{1}{4} \frac{d\langle x_1^2 \rangle}{dt} \right) - 4b_{12}\theta_{1s} \frac{d\langle x_1^2 \rangle}{dt} \quad (69)$$

Setting $y = d\langle x_1^2 \rangle/dt$, we obtain

$$\frac{dy}{y - \frac{a_{21}c_1}{a_{21} + 8b_{12}\theta_{1s}}} = - \left(\frac{a_{21}}{2} + 4b_{12}\theta_{1s} \right) dt \quad (70)$$

which, in turn, gives

$$\frac{d\langle x_1^2 \rangle}{dt} = y = c_3 \exp \left[- \left(\frac{a_{21}}{2} + 4b_{12}\theta_{1s} \right) t \right] + \frac{a_{21}c_1}{a_{21} + 8b_{12}\theta_{1s}} \quad (71)$$

or

$$\langle x_1^2 \rangle = - \left(\frac{2c_3}{a_{21} + 8b_{12}\theta_{1s}} \right) \exp \left[- \left(\frac{a_{21}}{2} + 4b_{12}\theta_{1s} \right) t \right] + \frac{a_{21}c_1}{a_{21} + 8b_{12}\theta_{1s}} t + c_4 \quad (72a)$$

Substituting $\langle x_1^2 \rangle$ into eqn. (68) gives

$$\langle x_2^2 \rangle = - \left(\frac{c_3}{a_{21} + 8b_{12}\theta_{1s}} \right) \exp \left[- \left(\frac{a_{21}}{2} + 4b_{12}\theta_{1s} \right) t \right] + \frac{2c_1 b_{12}\theta_{1s} t}{a_{21} + 8b_{12}\theta_{1s}} - \frac{c_4}{4} \quad (72b)$$

For the initial condition, $\langle x_1^2(0) \rangle$ and $\langle x_2^2(0) \rangle$ being zero at $t=0$, we conclude that

$$c_4 = 2c_3 / (a_{21} + 8b_{12}\theta_{1s})$$

On the other hand, $\langle x_1^2 \rangle$ and $\langle x_2^2 \rangle$ must satisfy eqns. (39) and (40) under any circumstances. Substitution of their expressions back into the governing equations gives the answers for c_1 and c_3 (see Appendix F)

$$c_1 = 6a_{21}\theta_{2s} \quad (73)$$

$$c_3 = \frac{4b_{12}\theta_{1s}^2(4b_{12}\theta_{1s} - a_{21})}{a_{21} + 8b_{12}\theta_{1s}} \quad (74)$$

Equations (72a) and (72b) represent the macroscopically steady-state solutions for the second moments of the fluctuating components. Recalling that the means of the fluctuating components, expressed as eqns. (63) and (64), converge to zero as time proceeds, we may use $\langle x_1^2 \rangle$ and $\langle x_2^2 \rangle$ as estimators for σ_1^2 and σ_2^2 , variances of the fluctuating components, by definition

$$\sigma_x^2 = \langle x^2 \rangle - \langle x \rangle^2 \quad (75)$$

When time approaches infinity, we see from eqns. (72a) and (72b) that σ_1^2 and σ_2^2 also approach infinity if the system is unbounded. This is in accordance with the expected behavior since the master equation expansion assumes that the process is Gaussian distributed on an unbounded state-space, whose variance is known to diverge linearly with time. However, for a bounded system which is physically realistic, it is expected that the maximum of the variance of the fluctuations is of

order of the system size. Therefore, the master equation expansion is valid for such a system sufficiently far from the boundaries. The time required for a stochastic system to reach its maximum randomness can be estimated from eqns. (72a) and (72b). It will be approximately equal to the time necessary for the variance to reach the system size, Ω . After this point, the original Fokker Planck equation resulting from the master equation expansion must be solved for the probability density function of the fluctuating component subject to appropriate boundary conditions, e.g., reflecting boundaries; we can no longer exploit the governing differential equations for the moments, e.g., eqns. (31) and (32), of the probability distribution.

3.6 DISCUSSION

It has been shown in this chapter that a fairly complete description of a stochastically behaving system can be obtained by the master equation modeling technique. The tenet of the proposed methodology manifested itself in two major steps.

Step 1. Imposition of the Markov property assumption and definition of the transition states of the system. This often gives rise to a discrete-state absolute probability balance equation, i.e., the master equation.

More often than not, the resultant master equation can not be solved explicitly. Thus, a systematic approach need be employed to find its approximate solution.

Step 2. Approximate solution through master equation expansion. This leads to a population balance equation and a Fokker-Planck equation.

In spite of its usefulness, implementation of the master equation expansion involves tedious manipulations. Among the difficult manipulations encountered are the transformation of the discrete-state master equation into its equivalent continuous form and the power series expansion of the random variable.

In this chapter, the methodology is illustrated with a simple example. Although real-world problems, e.g., the bubble behavior in the fluidized bed are far more complicated than this example, they can be modeled similarly. Upon the completion of the expansion, governing equations can be generated not only for the first and second moments discussed in this chapter, but also for the higher order and cross moments. Thus, information on the mean and fluctuating component of the system can be obtained by solving a sequence of these simultaneous differential equations. In principle, this can be implemented with the aid of digital computer; however, in reality, this may often be extremely difficult, if not impossible.

NOTATION

a, a^*	= bubble breakage rate constants defined in eqn. (A-9), $1/\text{cm}^3 \text{ sec}$
a^*	= ensemble bubble breakage rate constant defined in eqn. (B-10), $1/\text{cm}^3 \text{ sec}$
b, b^*	= bubble coalescence rate constants defined in eqn. (A-9), $1/\text{sec}$
b^*	= ensemble bubble coalescence rate constant defined in eqn. (B-10), $1/\text{sec}$
E_a^b	= step operator defined in eqns. (5) and (9)
$I(v-a)$	= index function
$n(V)$	= bubble size distribution function
$\{n\}$	= random number set representing a discrete bubble size distribution
n_i	= size distribution random number representing the number of bubbles of size i
$\{n_a\}, \{n_b\}$	= random number sets defined in Fig. 3
$\{n_c\}, \{n_d\}$	
$p(n, t)$	= probability density function, a continuous version of $P(\{n\}, t)$
$P(\{n\}, t)$	= probability of the systems to consist of a discrete bubble size distribution of $\{n\}$ at time t
t	= time, sec
V	= bubble volume, cm^3
x	= random variable defined in eqn. (20), $1/\text{cm}^{\frac{3}{2}}$
$\langle x \rangle$	= first moment of a random variable x
$\langle x^2 \rangle$	= second moment of random variable x

Greek Letters

- α = bubble breakage rate constant, 1/sec
- α^* = bubble breakage intensity defined in eqn. (3), 1/sec
- β = bubble coalescence rate constant, cm^3/sec
- β^* = bubble coalescence intensity defined in eqn. (3), 1/sec
- ϵ = infinitesimal volume element, cm^3
- ζ = the output rate of bubbles of sizes ranging from v to $v+dv$ per per unit volume
- ξ = parameter of the input rate of bubbles of sizes ranging from v to $v+dv$, $\Omega\xi(v)dv$
- π = probability density function defined in eqn. (21)
- ρ = bubble number density, $1/\text{cm}^3$
- Ω = system volume, cm^3

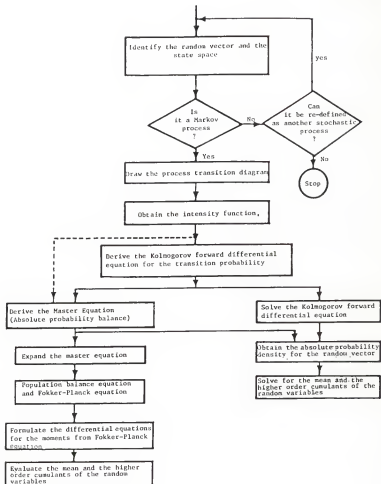


Fig. 3-1. Logistic flow chart for stochastic modeling.

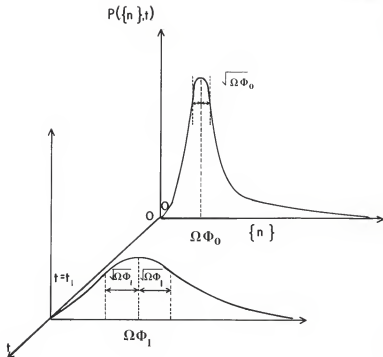
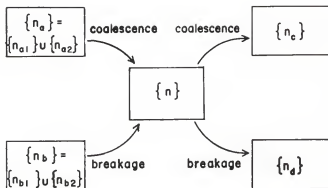


Fig. 3-2. $P(\{n\})-t$ relationship for illustrating the bubble size distribution in a dispersed bubbling system.



$$\begin{aligned} \{n\} &= \{n_1, n_2, \dots, n_i, \dots, n_{j-1}, \dots, n_j, \dots\} \\ \{n_{a1}\} &= \{n_1, n_2, \dots, n_i + 1, \dots, n_{j-1} + 1, \dots, n_j - 1, \dots\} \\ \{n_{a2}\} &= \{n_1, n_2, \dots, n_{j/2} + 2, \dots, n_j - 1, \dots\} \\ \{n_{b1}\} &= \{n_1, n_2, \dots, n_i - 1, \dots, n_{j-1} - 1, \dots, n_j + 1, \dots\} \\ \{n_{b2}\} &= \{n_1, n_2, \dots, n_{j/2} - 2, \dots, n_j + 1, \dots\} \end{aligned}$$

Fig. 3-3. Paths entering and leaving a reference state $\{n\}$ in a dispersed bubbling system.

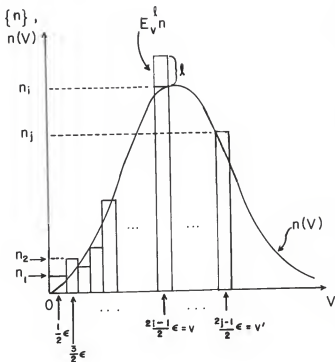


Fig. 3-4. Discrete function set $\{n\}$ and its continuous function form $n(V)$.

APPENDIX A

CONVERSION OF EQUATION (8) INTO A CONTINUOUS FORM, EQUATION (12)

To convert eqn. (8) into a continuous form, we let

$$\begin{aligned}v &= (i - \frac{1}{2})\epsilon \\v' &= (j - \frac{1}{2})\epsilon\end{aligned}\tag{A-1}$$

or

$$\begin{aligned}i &= \frac{v}{\epsilon} + \frac{1}{2} \\j &= \frac{v'}{\epsilon} + \frac{1}{2}\end{aligned}\tag{A-2}$$

The upper bound of the summation over i is

$$i = \frac{1}{2}(j - 1)\tag{A-3}$$

i.e.,

$$\frac{v}{\epsilon} + \frac{1}{2} = \frac{1}{2}\left(\frac{v'}{\epsilon} + \frac{1}{2} - 1\right)\tag{A-4}$$

or

$$v = \frac{2v' - 3\epsilon}{4}\tag{A-5}$$

The second and fourth terms of eqn. (8) can be rewritten, in continuous notation, respectively, as

$$\sum_{\omega=0}^{\infty} \sum_{v=\frac{\epsilon}{2}}^{\infty} \frac{\beta(v, \omega)}{\Omega} I(\omega - 2v) [E_v^2 E_{\omega}^{-1} - 1] n(v) [n(v) - 1] P(n(v), t)\tag{A-6}$$

and

$$\sum_{\omega=0}^{\infty} \sum_{v=\frac{\epsilon}{2}}^{\infty} \alpha(\omega, v) I(\omega - 2v) [E_v^{-2} E_{\omega}^1 - 1] n(\omega) P(n(v), t)\tag{A-7}$$

respectively. Here $I(\omega-2v)$ is an index function defined in eqn. (9) in the text. Equation (8) now becomes

$$\begin{aligned}
 \dot{P}(n,t) = & \sum_{v=\frac{\epsilon}{2}}^{\infty} \sum_{v'=\frac{\epsilon}{2}}^{\infty} \alpha(v',v) [E_v^{-1} E_{v'}^{-1} E_{v-v'}^{-1} - 1] n(v') P(n,t) \\
 & + \sum_{\omega=0}^{\infty} \sum_{v=\frac{\epsilon}{2}}^{\infty} \alpha(\omega,v) I(\omega-2v) [E_v^{-2} E_{\omega}^{-1} - 1] n(\omega) P(n,t) \\
 & + \sum_{v=\frac{\epsilon}{2}}^{\infty} \sum_{v'=\frac{\epsilon}{2}}^{\infty} \frac{2v'v-\epsilon}{4} \frac{\beta(v,v')}{\Omega} [E_v^{-1} E_{v'}^{-1} E_{v-v'}^{-1}] n(v) n(v'-v) P(n,t) \\
 & + \sum_{\omega=0}^{\infty} \sum_{v=\frac{\epsilon}{2}}^{\infty} \frac{\beta(v,\omega)}{\Omega} I(\omega-2v) [E_v^{-2} E_{\omega}^{-1} - 1] n(v) [n(v)-1] P(n,t)
 \end{aligned}
 \tag{A-8}$$

Here, $\alpha(*,*)$ and $\beta(*,*)$ are only variables which left defined in discrete form in the equation above. In order to complete the transformation, they need be redefined in continuous forms.

Let us set

$$\begin{aligned}
 a(v',v) &= \alpha(v',v)/\epsilon \\
 a^*(\omega,v) &= \alpha(\omega,v)/\epsilon \\
 b(v,v') &= \beta(v,v')/\epsilon \\
 b^*(v,\omega) &= \beta(v,\omega)/\epsilon
 \end{aligned}
 \tag{A-9}$$

under the condition that the following properties hold.

$$\begin{aligned}
 1) \quad & a(2v,v) = a(v,0) = 0 \\
 2) \quad & a^*(2v,v) = \frac{1}{2} \lim_{v' \rightarrow 2v} a(v',v) \\
 3) \quad & b(v,2v) = b(0,v) = 0 \\
 4) \quad & b^*(v,2v) = \frac{1}{2} \lim_{v' \rightarrow 2v} b(v,v')
 \end{aligned}
 \tag{A-10}$$

Taking limits as $\epsilon \rightarrow 0$ gives

$$\begin{aligned}
\dot{p}(n, t) = \lim_{\varepsilon \rightarrow 0} \frac{1}{\varepsilon} \left\{ \sum_{v'} \sum_v a(v', v) [E_v^{-1} E_{v'}^{-1} E_{-v}^{-1} E_v^1 - 1] n(v') p(n, t) \varepsilon \varepsilon \right. \\
+ \sum_{\omega} \sum_v a(\omega, v) I(\omega - 2v) [E_v^{-2} E_{\omega}^1 - 1] n(\omega) p(n, t) \varepsilon \varepsilon \\
+ \sum_{v'} \sum_v \frac{b(v, v')}{\Omega} [E_v^1 E_{v'}^1 E_{-v}^{-1} E_{v'}^{-1} - 1] n(v) n(v' - v) p(n, t) \varepsilon \varepsilon \\
+ \left. \sum_{\omega} \sum_v \frac{b(v, \omega)}{\Omega} I(\omega - 2v) [E_v^2 E_{\omega}^{-1} - 1] n(v) [n(v) - 1] p(n, t) \varepsilon \varepsilon \right\}
\end{aligned}$$

(A-10a)

or its equivalent continuous form

$$\begin{aligned}
\dot{p}(n, t) = \lim_{\varepsilon \rightarrow 0} \frac{1}{\varepsilon} \left\{ \int_0^{\infty} \int_0^{\frac{v'}{2}} a(v', v) [E_v^{-1} E_{v'}^{-1} E_{-v}^{-1} E_v^1 - 1] n(v') p(n, t) dv dv' \right. \\
+ \int_0^{\infty} \int_0^{\frac{v'}{2}} a^*(\omega, v) I(\omega - 2v) [E_v^{-2} E_{\omega}^1 - 1] n(\omega) p(n, t) dv d\omega \\
+ \int_0^{\infty} \int_0^{\frac{v'}{2}} \frac{b(v, v')}{\Omega} [E_v^1 E_{v'}^1 E_{-v}^{-1} E_{v'}^{-1} - 1] n(v) n(v' - v) p(n, t) dv dv' \\
+ \left. \int_0^{\infty} \int_0^{\frac{v'}{2}} \frac{b^*(v, \omega)}{\Omega} I(\omega - 2v) [E_v^2 E_{\omega}^{-1} - 1] n(v) [n(v) - 1] p(n, t) dv d\omega \right\}
\end{aligned}$$

(A-11)

which is identical to eqn. (12) in the text.

APPENDIX B

REARRANGEMENT OF EQUATION (28) TO A COMPACT FORM, EQUATION (30)

The partial derivatives incorporated with the term $\lim_{\varepsilon \rightarrow 0} \frac{1}{\varepsilon}$ in the right hand side of eqn. (28) can be expressed in terms of delta function, for example

$$\begin{aligned} \lim_{\varepsilon \rightarrow 0} \frac{1}{\varepsilon} \left[- \frac{\partial}{\partial x} \Big|_{V=V} - \frac{\partial}{\partial x} \Big|_{V=V'-V} + \frac{\partial}{\partial x} \Big|_{V=V} \right] \\ = \left[-\delta(V-V) - \delta(V-V'+V) + \delta(V-V') \right] \frac{\partial}{\partial x} \end{aligned} \quad (B-1)$$

where the delta function $\delta(V-a)$ is known as

$$\begin{aligned} \delta(V-a) &= \lim_{\varepsilon \rightarrow 0} \frac{1}{\varepsilon} I(V-a) \\ &= \begin{cases} \infty & @ V=a \\ 0 & \text{elsewhere} \end{cases} \end{aligned}$$

Therefore, write out eqn. (28) in the text in terms of delta functions and divide both sides of the equation by $-\frac{\partial \pi}{\partial x}$, we obtain

$$\begin{aligned} \frac{\partial \phi}{\partial t} &= \int_0^\infty \int_0^{\frac{V'}{2}} a(v', v) \delta(V-v) \phi(v') dv dv' \\ &+ \int_0^\infty \int_0^{\frac{V'}{2}} a(v', v) \delta(V-v'+v) \phi(v') dv dv' \\ &- \int_0^\infty \int_0^{\frac{V'}{2}} a(v', v) \delta(V-v') \phi(v') dv dv' \\ &+ 2 \int_0^\infty \int_0^\infty a^*(\omega, v) I(-2v) \delta(V-v) \phi(\omega) dv d\omega \\ &- \int_0^\infty \int_0^\infty a^*(\omega, v) I(\omega-2v) \delta(V-\omega) \phi(\omega) dv d\omega \\ &- \int_0^\infty \int_0^{\frac{V'}{2}} b(v, v') \delta(V-v) \phi(v) \phi(v'-v) dv dv' \end{aligned}$$

$$\begin{aligned}
& - \int_0^\infty \int_0^{\frac{v'}{2}} b(v, v') \delta(V - v' + v) \phi(v) \phi(v' - v) dv dv' \\
& + \int_0^\infty \int_0^{\frac{v'}{2}} b(v, v') \delta(V - v') \phi(v) \phi(v' - v) dv dv' \\
& - 2 \int_0^\infty \int_0^\infty b^*(v, \omega) I(\omega - 2v) \delta(V - v) \phi(v) \phi(v) dv d\omega \\
& + \int_0^\infty \int_0^\infty b^*(v, \omega) I(\omega - 2v) \delta(V - \omega) \phi(v) \phi(v) dv d\omega \quad (B-2)
\end{aligned}$$

By changing the sequence of integration into a suitable order, we can first perform the integration with respect to the delta function for each term in the right hand side of eqn. (B-2). For instance, consider the first term in the right hand side of eqn. (B-2), we obtain

$$\begin{aligned}
& \int_0^\infty \int_0^{\frac{v'}{2}} a(v', v) \delta(V - v) \phi(v') dv dv' \\
& = \int_0^\infty \int_{2v}^\infty a(v', v) \delta(V - v) \phi(v') dv' dv \\
& = \int_{2V}^\infty a(v', V) \phi(v') dv' \quad (B-3)
\end{aligned}$$

Next, for the second term

$$\begin{aligned}
& \int_0^\infty \int_0^{\frac{v'}{2}} a(v', v) \delta(V - v' + v) \phi(v') dv dv' \\
& = \int_0^\infty \int_0^u a(u+v, u) \delta(V - u) \phi(u+v) dv du \quad (u = v' - v) \\
& = \int_0^V a(V+v, V) \phi(V+v) dv \\
& = \int_V^{2V} a(v', V) \phi(v') dv' \quad (v' = V+v) \quad (B-4)
\end{aligned}$$

Performing the integration term by term leads to

$$\begin{aligned}
 \frac{\partial \phi}{\partial t} = & \int_{2V}^{\infty} a(v', V) \phi(v') dv' + \int_V^{2V} a(v', V) \phi(v') dv' \\
 & - \int_0^{\frac{V}{2}} a(V, v) \phi(V) dv + 2 \int_0^{\infty} a^*(\omega, V) I(\omega - 2V) \phi(\omega) d\omega \\
 & - \int_0^{\infty} a^*(V, v) I(V - 2v) \phi(V) dv \\
 & - \int_V^{\infty} b(V, V+v) \phi(V) \phi(v) dv \\
 & - \int_0^V b(V, V+v) \phi(v) \phi(V-v) dv \\
 & + \int_0^{\frac{V}{2}} b(v, V) \phi(v) \phi(V-v) dv \\
 & - 2 \int_0^{\infty} b^*(V, \omega) I(\omega - 2V) \phi(V) \phi(\omega) d\omega \\
 & + \int_0^{\infty} b^*(v, V) I(V - 2v) \phi(v) \phi(V) dv
 \end{aligned} \tag{B-5}$$

or in a more compact form

$$\begin{aligned}
 \frac{\partial \phi}{\partial t} = & \int_V^{\infty} a(v', V) \phi(v') dv' + 2 \int_0^{\infty} a^*(\omega, V) I(\omega - 2V) \phi(\omega) d\omega \\
 & - \int_0^{\frac{V}{2}} a(V, v) \phi(V) dv - \int_0^V a^*(V, v) I(V - 2v) \phi(V) dv \\
 & - \int_0^{\infty} b(V, V+v) \phi(V) \phi(v) dv - 2 \int_0^{\infty} b^*(V, \omega) I(\omega - 2V) \phi^2(V) d\omega \\
 & + \int_0^{\frac{V}{2}} b(v, V) \phi(v) \phi(V-v) dv + \int_0^V b^*(v, V) I(V - 2v) \phi^2(v) dv
 \end{aligned} \tag{B-6}$$

from which

$$\begin{aligned}
 \frac{\partial \phi}{\partial t} = & \int_V^{\infty} [a(v, V) + 2a^*(v, V) I(V - 2v)] \phi(v) dv \\
 & - \frac{1}{2} \int_0^V [a(V, v) + 2a^*(V, v) I(V - 2v)] \phi(V) dv \\
 & + \int_0^{\frac{V}{2}} [b(v, V) + 2b^*(v, V) I(V - 2v)] \phi(v) \phi(V-v) dv
 \end{aligned}$$

$$- \int_0^{\infty} [b(V, V+v) + 2b^*(V, V+v)I(V-v)]\phi(V)\phi(v)dv \quad (B-7)$$

In derivations above, we make use of the property that in $a(j, i)$ and $b(i, j)$, the value of i cannot exceed that of j . Also realized is the relation

$$\int_0^V b^*(v, V)dv = 2 \int_0^{\frac{V}{2}} b^*(v, V)dv \quad (B-8)$$

By definitions of $a(j, i)$, $a^*(j, i)$, $b(i, j)$ and $b^*(i, j)$ shown in eqn.

(A-10), eqn (B-7) is understood to be

$$\begin{aligned} \frac{\partial \phi}{\partial t} = & \int_V^{\infty} a'(v, V)\phi(v)dv - \frac{1}{2} \int_0^V a'(V, v)\phi(V)dv \\ & + \int_0^{\frac{V}{2}} b'(v, V)\phi(v)\phi(V-v)dv \\ & - \int_0^{\infty} b'(V, V+v)\phi(V)\phi(v)dv \end{aligned} \quad (B-9)$$

where

$$\begin{aligned} a'(v, V) &= a(v, V) + I(V-2V) \lim_{v \rightarrow 2V} a(v, V) \\ a'(V, v) &= a(V, v) + I(V-2v) \lim_{V \rightarrow 2v} a(V, v) \\ b'(v, V) &= b(v, V) + I(V-2V) \lim_{V \rightarrow 2v} b(v, V) \\ b'(V, V+v) &= b(V, V+v) + I(V-v) \lim_{V \rightarrow v} b(V, V+v) \end{aligned} \quad (B-10)$$

Equation (B-9) is identical to eqn. (30) in the text.

APPENDIX C

DERIVATIONS OF EQUATIONS (31) AND (32)

Rewrite eqn. (29) in terms of delta function as discussed in
APPENDIX B,

$$\begin{aligned}
 \frac{\partial \pi}{\partial t} = & \int_0^\infty \int_0^{\frac{v'}{2}} a(v', v) [-\delta(V-v) - \delta(V-v'+v) + \delta(V-v')] \frac{\partial}{\partial x} [x(v') \pi] dv dv' \\
 & + \int_0^\infty \int_0^\infty a^*(\omega, v) I(\omega-2v) [-2\delta(V-v) + \delta(V-\omega)] \frac{\partial}{\partial x} [x(\omega) \pi] dv d\omega \\
 & + \int_0^\infty \int_0^{\frac{v'}{2}} b(v, v') [\delta(V-v) + \delta(V-v'+v) - \delta(V-v')] \\
 & \quad \frac{\partial}{\partial x} [\theta(v) x(v'-v) + \theta(v'-v) x(v)] \pi dv dv' \\
 & + \int_0^\infty \int_0^\infty b^*(v, \omega) I(\omega-2v) [2\delta(V-v) - \delta(V-\omega)] \frac{\partial}{\partial x} [2\theta(v) x(v)] \pi dv d\omega \\
 & + \frac{1}{2} \int_0^\infty \int_0^{\frac{v'}{2}} [\delta(V-v) + \delta(V-v'+v) + \delta(V-v')] \\
 & \quad \frac{\partial^2}{\partial x^2} [a(v', v) \theta(v') \pi + b(v, v') \theta(v) \theta(v'-v) \pi] dv dv' \\
 & + \frac{1}{2} \int_0^\infty \int_0^\infty I(\omega-2v) [4\delta(V-v) + \delta(V-\omega)] \frac{\partial^2}{\partial x^2} [a^*(\omega, v) \theta(\omega) \pi \\
 & \quad + b^*(v, \omega) \theta^2(v) \pi] dv d\omega \quad (C-1)
 \end{aligned}$$

Integrating this equation term by term and utilizing the property of the delta function gives

$$\begin{aligned}
 \frac{\partial \pi}{\partial t} = & \int_{2V}^\infty -a(v', V) \frac{\partial}{\partial x} [x(v') \pi] dv' \\
 & - \int_V^{2V} a(v', V) \frac{\partial}{\partial x} [x(v') \pi] dv'
 \end{aligned}$$

$$\begin{aligned}
& + \int_0^V \frac{1}{2} a(V, v) \frac{\partial}{\partial x} [x(V) \pi] dv \\
& - 2 \int_0^\infty a^*(\omega, V) I(\omega - 2V) \frac{\partial}{\partial x} [x(\omega) \pi] d\omega \\
& + \int_0^\infty a^*(V, v) I(V - 2v) \frac{\partial}{\partial x} [x(V) \pi] dv \\
& + \int_V^\infty b(V, V+v) \frac{\partial}{\partial x} [\phi(V) x(v) + \phi(v) x(V)] \pi dv \\
& + \int_0^V b(V, V+v) \frac{\partial}{\partial x} [\phi(V) x(v) + \phi(v) x(V)] \pi dv \\
& - \int_0^V \frac{1}{2} b(v, V) \frac{\partial}{\partial x} [\phi(v) x(V-v) + \phi(V-v) x(v)] \pi dv \\
& + 4 \int_0^\infty b^*(V, \omega) I(\omega - 2V) \frac{\partial}{\partial x} [\phi(V) x(V)] \pi d\omega \\
& - 2 \int_0^\infty b^*(v, V) I(V - 2v) \frac{\partial}{\partial x} [\phi(v) x(v)] \pi dv \\
& + \frac{1}{2} \int_{2V}^\infty a(v', V) \frac{\partial^2}{\partial x^2} [\phi(v') \pi] dv' \\
& + \frac{1}{2} \int_V^{2V} a(v', V) \frac{\partial^2}{\partial x^2} [\phi(v') \pi] dv' \\
& + \frac{1}{2} \int_0^V \frac{1}{2} a(V, v) \frac{\partial^2}{\partial x^2} [\phi(V) \pi] dv \\
& + \frac{4}{2} \int_0^\infty a^*(\omega, V) I(\omega - 2V) \frac{\partial^2}{\partial x^2} [\phi(\omega) \pi] d\omega \\
& + \frac{1}{2} \int_0^\infty a^*(V, v) I(V - 2v) \frac{\partial^2}{\partial x^2} [\phi(V) \pi] dv \\
& + \frac{1}{2} \int_V^\infty b(V, V+v) \frac{\partial^2}{\partial x^2} [\phi(V) \phi(v) \pi] dv \\
& + \frac{1}{2} \int_0^V b(V, V+v) \frac{\partial^2}{\partial x^2} [\phi(V) \phi(v) \pi] dv \\
& + \frac{1}{2} \int_0^V \frac{1}{2} b(v, V) \frac{\partial^2}{\partial x^2} [\phi(v) \phi(V-v) \pi] dv
\end{aligned}$$

$$\begin{aligned}
& + \frac{4}{2} \int_0^\infty b^*(v, \omega) I(\omega - 2v) \frac{\partial^2}{\partial x^2} [\theta^2(v) \pi] d\omega \\
& + \frac{1}{2} \int_0^\infty b^*(v, v) I(v - 2v) \frac{\partial^2}{\partial x^2} [\theta^2(v) \pi] dv
\end{aligned} \quad (C-2)$$

In order to derive equations for the moments of the random variable x , we need the following integrations,

$$\begin{aligned}
1) \quad \int_{-\infty}^{\infty} x(V) \frac{\partial}{\partial t} dx &= \frac{\partial}{\partial t} \int_{-\infty}^{\infty} x(V) \pi(x, t) dx \\
&= \frac{\partial \langle x(V) \rangle}{\partial t} \\
2) \quad \int_{-\infty}^{\infty} x(V) \frac{\partial [x(V) \pi]}{\partial t} dx &= x(V) \pi(V) \pi \Big|_{-\infty}^{\infty} - \int_{-\infty}^{\infty} x(V) \pi dx \\
&= -\langle x(V) \rangle \\
3) \quad \int_{-\infty}^{\infty} x(V) \frac{\partial^2}{\partial x^2} dx &= x(V) \frac{\partial \pi}{\partial x} \Big|_{-\infty}^{\infty} - \int_{-\infty}^{\infty} \frac{\partial \pi}{\partial x} dx \\
&= -\pi \Big|_{-\infty}^{\infty} = 0
\end{aligned}$$

Similarly,

$$\begin{aligned}
4) \quad \int_{-\infty}^{\infty} x(V)^2 \frac{\partial \pi}{\partial t} dx &= \langle x(V)^2 \rangle \\
5) \quad \int_{-\infty}^{\infty} x(V)^2 \frac{\partial [x(V) \pi]}{\partial x} dx &= -2 \langle x(V)^2 \rangle \\
6) \quad \int_{-\infty}^{\infty} x(V)^2 \frac{\partial^2 \pi}{\partial x^2} dx &= 2
\end{aligned}$$

where $\langle x \rangle$ stands for the first moment of x , and $\langle x^2 \rangle$ the second moment.

Multiplying both sides of eqn. (C-2) by $x(V)$ and subsequently integrating the resultant equation with respect to x over the range of $(-\infty, \infty)$ term by term, we obtain the equation for the first moment of x , i.e.,

$$\begin{aligned}
 \frac{d\langle x(V) \rangle}{dt} = & \int_V^\infty [a(v', V) + 2a^*(v', V)I(v' - 2V)] \langle x(v') \rangle dv' \\
 & - \frac{1}{2} \int_0^V [a(V, v) + 2a^*(V, v)I(V - 2v)] \langle x(v) \rangle dv \\
 & + \int_0^{\frac{V}{2}} [b(v, V) + 2b^*(v, V)I(V - 2v)] [\phi(v) \langle x(V - v) \rangle + \\
 & \quad + \phi(V - v) \langle x(v) \rangle] dv \\
 & - \int_0^\infty [b(V, V + v) + 2b^*(V, V + v)I(V - v)] [\phi(v) \langle x(v) \rangle + \\
 & \quad + \phi(v) \langle x(V) \rangle] dv
 \end{aligned} \tag{C-3}$$

Multiplying both sides of eqn. (C-2) by $x(V)^2$ and subsequently integrating the resultant equation with respect to x over the range of $(-\infty, \infty)$, we obtain the equation for the second moment of x , i.e.,

$$\begin{aligned}
 \frac{\partial \langle x(V)^2 \rangle}{\partial t} = & 2 \int_V^\infty a'(v', V) \langle x(v')^2 \rangle dv' \\
 & - \int_0^V a'(V, v) \langle x(v)^2 \rangle dv \\
 & + 2 \int_0^{\frac{V}{2}} b'(v, V) [\phi(v) \langle x(V - v)^2 \rangle + \phi(V - v) \langle x(v)^2 \rangle] dv \\
 & - 2 \int_0^\infty b'(V, V + v) [\phi(V) \langle x(v)^2 \rangle + \phi(v) \langle x(V)^2 \rangle] dv \\
 & + \int_V^\infty a'(v', V) \phi(v') dv \\
 & + \frac{1}{2} \int_0^V a'(V, v) \phi(v) dv
 \end{aligned}$$

$$\begin{aligned}
& + \int_0^{\frac{V}{2}} b'(v, V) \phi(v) \phi(V-v) dv \\
& + \int_0^{\infty} b'(v, V+v) \phi(V) \phi(v) dv
\end{aligned} \tag{C-4}$$

Here, eqns. (C-3) and (C-4) are the same as eqns. (31) and (32), respectively, in the text.

APPENDIX D

SOLUTION FOR EQUATION (45)

Rewriting eqn. (45), we have

$$\frac{d\phi_1}{dt} = a\phi_1^2 + b\phi_1 + c \quad (D-1)$$

where

$$a = -b_{12}$$

$$b = \frac{-a_{21}}{2}$$

$$c = \frac{a_{21}N_1}{2\Omega}$$

With the fact that $b^2 - 4ac > 0$, we have the solution for eqn. (D-1) from integration table

$$t = \frac{1}{a(p-q)} \ln \left[\frac{(\phi_1 - p)(\phi_0 - q)}{(\phi_1 - q)(\phi_0 - p)} \right] \quad (D-2)$$

where

$$p = A + B \quad (D-3)$$

$$q = A - B \quad (D-4)$$

$$A = -\frac{a_{21}}{4b_{12}} \quad (D-5)$$

$$B = \frac{1}{2} \left(\frac{a_{21}}{2b_{12}} \right)^2 + \frac{2a_{21}N_1}{b_{12}\Omega} \quad (D-6)$$

$$\phi_0 = \phi_1(0) \quad (D-7)$$

From eqns. (D-3) and (D-4), we obtain

$$a(p-q) = -2Bb_{12}$$

Thus, eqn. (D-2) can be rewritten as

$$e^t = \left[\frac{(\phi_1 - p)(\phi_0 - q)}{(\phi_1 - q)(\phi_0 - p)} \right] \frac{-1}{2Bb_{12}} \quad (D-8)$$

or

$$\phi_1 = \frac{(A-B)[\phi_0 - (A+B)]e^{-2Bb_{12}t} - (A+B)[\phi_0 - (A-B)]}{[\phi_0 - (A+B)]e^{-2Bb_{12}t} - [\phi_0 - (A-B)]} \quad (D-9)$$

Equation (D-9) is an equivalent expression for eqn. (46) in the text.

APPENDIX E

STEADY STATE SOLUTION FOR EQUATION SET (37a) AND (37b)

To obtain the steady state solutions for the macroscopic bubble number densities, ϕ_{1s} and ϕ_{2s} , the left hand sides of eqns. (35) and (36) are set to zero. The resultant equations are identical to each other; it is of the form

$$\phi_{2s} = \frac{b_{12}}{a_{21}} \phi_{1s}^2 \quad (E-1)$$

The volume conservation gives

$$N_1 = \phi_{1s} \Omega + 2\phi_{2s} \Omega \quad (E-2)$$

Merging eqns. (E-1) and (E-2) yields a quadratic equation of ϕ_{1s}

$$2b_{12}\Omega\phi_{1s}^2 + a_{21}\Omega\phi_{1s} - a_{21}N_1 = 0 \quad (E-3)$$

from which ϕ_{1s} is solved to be

$$\phi_{1s} = \frac{-a_{21}\Omega + a_{21}^2\Omega^2 + 8a_{21}b_{12}N_1\Omega}{4b_{12}\Omega} \quad (E-4)$$

APPENDIX F

SOLUTION FOR CONSTANTS c_1 AND c_3 IN EQUATION (71)

By summing eqn. (39) and 4 times eqn. (40) at macroscopic steady-state, we have

$$\frac{d\langle x_1^2 \rangle}{dt} + 4 \frac{d\langle x_2^2 \rangle}{dt} = 3a_{21}\phi_{2s} + 3b_{12}\phi_{1s}^2 \quad (F-1)$$

Replacing $\langle x_1^2 \rangle$ and $\langle x_2^2 \rangle$ with eqns. (72a) and (72b), respectively, we obtain

$$\begin{aligned} c_1 &= 3(a_{21}\phi_{2s} + b_{12}\phi_{1s}^2) \\ &= 6a_{21}\phi_{2s} \end{aligned} \quad (F-2)$$

Next, by direct substitution of eqns. (72a) and (72b) into eqn. (39), we obtain

$$\begin{aligned} c_3 \exp\left[-\left(\frac{a_{21}}{2} + 4b_{12}\phi_{1s}\right)t\right] &+ \frac{a_{21}c_1}{a_{21} + 8b_{12}\phi_{1s}} \\ &= \frac{(a_{21} + 8b_{12}\phi_{1s})c_3}{a_{21} + 8b_{12}\phi_{1s}} \exp\left[-\left(\frac{a_{21}}{2} + 4b_{12}\phi_{1s}\right)t\right] \\ &+ \frac{4a_{21}c_1b_{12}\phi_{1s}t - 4a_{21}c_1b_{12}\phi_{1s}^2t}{a_{21} + 8b_{12}\phi_{1s}} \\ &- \frac{(a_{21} + 8b_{12}\phi_{1s})c_3}{(a_{21} + 8b_{12}\phi_{1s})} + a_{21}\phi_{2s} + b_{12}\phi_{1s}^2 \end{aligned} \quad (F-3)$$

or

$$c_3 = 2a_{21}\phi_{2s} - \frac{a_{21}c_1}{a_{21} + 8b_{12}\phi_{1s}}$$

$$\begin{aligned}
&= 2a_{21}\theta_{2s} - \frac{6a_{21}^2\theta_{2s}}{a_{21}+8b_{12}\theta_{1s}} \\
&= \frac{4b_{12}\theta_{1s}^2(4b_{12}\theta_{1s}-a_{21})}{a_{21}+8b_{12}\theta_{1s}} \quad (F-4)
\end{aligned}$$

CHAPTER 4

PRESSURE FLUCTUATIONS IN A GAS-SOLID FLUIDIZED BED WITH A SCREEN

To enhance the fundamental understanding of the effect of screen packings on the performance of the gas-solid fluidized bed in terms of pressure fluctuations, the simplest configuration, a single screen installed across the entire section of the bed, was investigated in this chapter. The effect of the screen insertion on the performance of the bed was determined qualitatively by calculating on-line statistical parameters of the pressure fluctuations.

4.1. EXPERIMENTAL

The experimental facilities and procedures are presented in this section.

Facilities

The arrangement of equipment is shown in Fig. 4-1. The fluidized bed employed consisted of a bed proper, a distributor and a plenum column. The bed proper and plenum, were fabricated from "plexiglas" to permit visual observation. Their diameter was 0.203 m (8 in) and their heights were 0.61 m (24 in) and 0.17 m (6.7 in), respectively. The layout of holes in the distribution is shown in Fig. 4-2. The bed proper consisted of four bed columns connected by flanges; each was 0.15 m (6 in) long. A stainless steel wire screen was inserted between two columns 0.15 m above the perforated distributor so that the screen could be changed easily for testing on the pressure fluctuations. The fluidized particles were 0.000491 m in diameter within a narrow cut of the U.S. Standard Sieve No. -30 ~ +40. The density of the sand was 2620 kg/m³. Air with a temperature of approximately 40±5°C served as the fluidizing medium.

A pressure tap was installed on the wall of the bed column immediately above the distributor. The inside opening of the tap was covered with a screen to prevent the sand from entering the tap. The outside opening of the tap was connected to one of the two input channels of a differential pressure transducer (Enterprise Model CJ3D), which produced an output voltage proportional to the pressure difference between two channels. The remaining channel was exposed to the atmosphere, and thus, the fluctuations of pressure drop across the entire bed were measured. The working capacity of the transducer was ±6.90 KPa (+ 1 psi).

The calculating and recording assembly included a correlation and probability analyzer (Honeywell Model SAI-43A), a Fourier transform analyzer (Honeywell Model SAI-470), a strip chart recorder, an X-Y plotter and two oscilloscopes.

All the components of the calculating and recording assembly were calibrated extensively prior to the experiments. The pressure probe was disconnected from the fluidized bed and connected to a manometer as shown in Fig. 4.1. The manometer served as a standard pressure signal source. Manipulating it varied pressure signals transmitted to the strip chart recorder and correlation and probability analyzer from the pressure transducer (see Appendix A for details).

After calibration, the pressure probe was detached from the manometer and connected to the fluidized bed. A test run was made to determine the minimum fluidization velocity. It was found to conform to the value calculated by the Ergun equation (also see Appendix A).

Procedure

For each run of the experiment, the pressure fluctuations of the bed with or without the screen were detected by connecting the tap to the pressure transducer. The voltage-time signal (corresponding to the pressure-time signal) from the transducer was sent to both the strip chart recorder and the correlation and probability analyzer; the former registered the pressure-time signal, and the latter calculated on-line the auto-correlation and probability distribution functions of the signal. The sampling interval for calculation was selected to be 10 ms, and a total of 64×1024 points were sampled. The Fourier transform

analyzer transformed the auto-correlation function in the time domain into the corresponding power spectral density function in the frequency domain [see Eqn. (B-6) in Appendix B]. The calculated results were observed on the oscilloscopes and also recorded on the X-Y plotter.

From these calculations, the mean of pressure fluctuations and the variance and major frequency of pressure fluctuations, which were considered as indices of instability of the bed, were recovered. The probability distribution function, calculated using DC coupling mode of the correlation and probability analyzer, was employed to determine the mean of pressure fluctuations. It was accomplished by reading the X-axis value of the $F_{X(t)}(0.5)$ point, since the pressure fluctuations are assumed to be normally distributed. The auto-correlation function of the pressure fluctuation signal at the zero time shift gave its variance. The major frequency of pressure fluctuations was determined from locating the maximim peak of their power spectral density function.

4.2 RESULTS AND DISCUSSION

Experimental results, both without screen and with a single screen, are summarized in Tables 4-1 and 4-2 as well as Fig. 4-3.

Qualitative Observation

Figures 4-4 through 4-7 show examples of pressure-time curves without screen and with a single screen of 8 x 8, 12 x 14 or 20 x 20 mesh. The case without a screen corresponds to the very large ratio of the screen opening to the average diameter of particles. The screen with a size of 8 x 8, 12 x 14, or 20 x 20 mesh corresponds to the ratio of 5, 3, or 2. Examples of their auto-correlation functions and power spectral density functions are illustrated in Figs. 4-8 and 4-9 , respectively , in which

the minimum fluidization velocity, U_{mf} , the corresponding bed height, H_{mf} , and the normalized velocity, U/U_{mf} , were 0.25 m/sec., 0.11 m and 3.0, respectively. Recall that the location of the screen, installed across the entire section of the bed, was 0.15 m above the distributor

A example of the pressure-time curve without a screen is presented in Fig. 4-4; its corresponding auto-correlation function and power spectral density are presented in Figs. 4-8 and 4-9, respectively. The auto-correlation function has a damped sinusoidal shape and the power spectral density function exhibits a sharp peak. Both are relevant for identifying a periodic component in the fluctuations (Lirag and Littman, 1971; Fan *et al.*, 1981).

An example of the pressure fluctuations in the bed with an 8 x 8 mesh screen ($R \approx 5$) is shown in Fig. 4-5; the corresponding auto-correlation function and power spectral density are also presented in Figs. 4-8 and 4-9, respectively. The pressure-time curve appears to contain relatively small fluctuations of a high frequency with momentary jumps superimposed on them. A visual observation shows the screen is completely immersed in the bed and no segregation is observed. The bed expansion is reduced as shown in Fig. 4-10. The amplitude of fluctuations is smaller than that in Fig. 4-4. It means that the stability of the bed has been improved. The evidence of enhanced stability can also be seen from the auto-correlation function and power spectral density function; the amplitudes of the auto-correlation function are smaller than those for the bed without screen (Fig. 4-8). Also, the major frequencies increase slightly compared to the case without screen.

The momentary jumps probably can be attributed to the wall effect of the screen. The mobility of particles is reduced by the walls of the screen openings leading alternatively to local blockage of opening and spurting at the top of the bed. As the screen openings become finer, the screen effect will vary in response to the velocity change on the behavior of the fluidized bed.

Figure 4-6 illustrates typical pressure fluctuations at a moderate fluidizing velocity ($U/U_{mf}=3$) with a screen of the size 12 x 14 mesh ($R \approx 3$). The pressure-time curve appears to contain relatively small fluctuations of a high frequency, ca 3.8Hz, with momentary jumps superimposed on them as in the case in Fig. 4-5. However, the amplitude of the jumps is appreciably greater than that in Fig. 4-5, but the frequency of the jumps, ca 0.35 Hz, is much lower than that in Fig. 4-5. It was observed that a very thin layer of packed section was formed momentarily beneath the screen followed by its gradual migration through the screen. When the packed section was suddenly formed, the fluctuations jumped to a high pressure level; when the packed section gradually moved across the screen, the fluctuations slid back to the original level until the next jump occurred. A shallow fluidized section existed above the screen and spurting happened frequently at the top part of the bed while the packed section was not formed beneath the screen. The momentary jumps probably can be attributed to appreciable wall effect of the screen openings, thus leading to the formation of the packed section across the entire cross-section of the bed beneath the screen.

At a relatively high air velocity ($U/U_{mf} > 3$), the mean pressure drop across the bed with a screen of the size of 12 x 14 mesh drops significantly as shown in Fig. 4-3. This was due to the fact after the air broke through locally the packed section beneath and the shallow fluidized section above the screen, the packed section would disappear but a fairly substantial amount of sand would remain on the screen. Hereafter, the fluidizing air would continue to "by-pass", and thus the sand remained on the screen would not contribute to the pressure drop across the entire bed.

As shown in Fig. 4-7, a 20 x 20 mesh screen ($R = 2$) generates a high pressure drop, fluctuating with a high frequency and a small amplitude. Though the openings of this screen were still larger than the average diameter of the fluidized sand, they would be easily blocked by the sand due to the non-uniformity in particle size or bridging. A packed section was thus formed, which in turn increased the pressure drop. The packed section became thicker as the air velocity increased, similar to the operation of a semi-fluidized bed. The pressure drop then increased correspondingly. This phenomenon can be observed in Fig. 4-3.

Another interesting phenomenon worth noting in the case of a 20 x 20 mesh screen occurred at a certain air velocity. Figure 4-11 shows that a screen of 20 x 20 mesh ($R = 2$) generates a pressure-time signal of an almost periodic wave of a low frequency and a large amplitude, superimposed on essentially random fluctuations of a high frequency and a low amplitude. It was observed that a packed section was formed gradually beneath the screen, followed by its gradual collapse; a shallow fluidized section was always present above the screen and no spurting was observed. The period of the relatively low frequency wave was approximately 3.7 min.; this is equivalent to a frequency of 4.50×10^{-3} Hz. This frequency was

too low to be recovered in the power spectral density function calculated on line because it was beyond the range of the Fourier transform analyzer in use. This phenomenon probably can be explained as follows: When the screen openings are reduced, the wall effect is enhanced. Consequently, a relatively stable fluidized bed is formed above the screen, and the particles are exchanged slowly between the fluidized section above the screen and the packed section beneath the screen. Furthermore, the gas velocity distribution is rendered uniform by the screen, the packed section beneath it and the fluidized section above it.

Figure 4-8 shows that a decrease in the size of screen openings reduces the amplitudes of the auto-correlation functions of pressure fluctuations. Fig. 4-9 shows that peaks of the power spectral density functions shift slightly to the right with the decrease in the screen openings. Both results indicate that the stability of the bed has been improved. Furthermore, we see that a small hump appears in the low frequency side near the main peak when a screen with relatively small openings, e.g., 12 x 14 mesh or 20 x 20 mesh, was inserted across the bed. This can probably be attributed to the formation of a relatively stable fluidized section above the screen; this section redistributes the bubbles.

Screen Effect on the Bed Performance

It has been noticed that the statistical properties of pressure fluctuations, such as the major frequency and the inverse of the amplitude, can be employed as indices of bed performance (Song *et al.*, 1984). A bed with pressure fluctuations of high frequency is considered to have numerous fast-moving bubbles which improve the bed quality, e.g., increase the heat and mass transfer rates. A bed with pressure fluctuations of small variance is considered to have

a stable flow pattern which enhance the bed stability (Winter, 1968). The major frequency and variance of pressure fluctuations are plotted as functions of the normalized gas velocity in Figs. 4-12 and 4-13, respectively. The parameters in these figures are the screen size and the ratio of the screen opening to the average diameter of particles. We see that under full fluidization (without a screen), the variance of pressure fluctuations is a monotonic increasing function of the normalized gas velocity while the major frequency remained constant.

As stated previously, a single screen was installed across the entire cross-section of the bed at 0.15 m above the distributor. The bed reached this position of the screen approximately at $U/U_{mf} = 2.2$. As expected, the screen did not appreciably influence the two indices of the bed performance when the normalized velocity was smaller than this value. When the normalized air velocity exceeded the threshold value of $U/U_{mf} = 2.2$, the bed expansion reached the screen. Under this condition, the variance of pressure fluctuations increased with an increase in the normalized air velocity at a much smaller rate than that of the bed without screen. Meanwhile, the major frequency of pressure fluctuations increased with an increase in the air velocity, thereby indicating the enhancement of the bed quality as well as stability. This eventually resulted in fluctuations with a relatively small amplitude and a high frequency. In other words, for a given particle size, the smaller the size of screen openings, the lower the variance value and the higher the major frequency.

The screen effect on the bed performance can be explained as followed:

- (a) The screen breaks up the bubbles, thus diminishing the pressure fluctuations.

- (b) Due to the wall effect of screen openings, the mobility of particles will be reduced when the openings are small (Kang et al., 1967; Winter, 1968); this should result in variation in the dense phase porosity.
- (c) The gas velocity distribution is rendered uniform not only by the screen but also by the packed section beneath the screen and the fluidized section above the screen when the screen opening are relatively small (12 x 14 mesh and 20 x 20 mesh).

In addition to its contribution to bed quality as well as stability, the insertion of a screen in the fluidized bed causes other effects, such as reduced bed expansion, segregation of the bed into a fluidized section and a packed section above it, and formation of a shallowed fluidized bed above the screen. These concomitant effects can be advantages or disadvantages to the fluidized-bed operation depending on its application. Hence, caution must be exercised in selecting the screen size for the purpose of improving the performance of a gas-solid fluidized bed.

NOTATION

A	= cross sectional area of a fluidized bed, cm^2
\bar{d}_p	= average diameter of the fluidized particles, cm
D_b	= diameter of the fluidized bed, cm
$f_{X(t)}(x)$	= probability function
$F_{X(t)}(x)$	= cumulative probability distribution function
g	= gravitational constant, cm/sec^2
G	= variable defined in eqn. (A-1), V
H	= bed expansion height, m
H_{mf}	= bed expansion height at the minimum fluidization velocity, m
k	= constant in eqn. (A-1)
K	= settling criterion defined in eqn. (A-3)
L, h	= readings from the X-Y plotter, cm
P	= pressure drop, KPa
R	= ratio of the screen opening to the average diameter of particles
Re_p	= particle Reynolds number
$R_{xx}(t)$	= auto correlation function
S	= sensitivity setting of the X-Y plotter, mV/cm
$S_{xx}(W)$	= power spectral density function
T	= time, sec
U	= linear air velocity, m/sec
U_{mf}	= minimum fluidization velocity, m/sec
W	= total weight of the fluidized particles, g

GREEK

μ	= mean
μ_g	= viscosity of the fluidizing gas, g/cm sec
ρ_g	= density of the fluidizing air, g/cm ³
ρ_p	= density of the fluidized particles, g/cm ³
σ^2	= variance

Table 4-1. Experimental results showing the screen effect on the major frequency of pressure fluctuations in the fluidized bed.

$\frac{U}{U_{mf}}$	Major Frequency (Hz)			
	Without screen	8x8 mesh screen	12x14 mesh screen	20x20 mesh screen
1.4	3.85	3.9	3.9	3.85
1.5	3.75	3.9	3.8	3.75
1.7	3.75	3.9	3.8	3.75
2.2	3.65	3.9	3.7	3.65
2.4	3.65	3.9	3.7	3.65
2.6	3.65	3.9	3.7	3.65
2.9	3.65	3.9	3.7	.0005/4.0
3.1	3.65	3.8	0.35/3.75	4.55
3.3	3.65	4.5	0.35/4.0	4.5

Table 4-2. Experimental results showing the screen effect on the variance of pressure fluctuations in the fluidized bed.

$\frac{U}{U_{mf}}$	Variance $\times 10^3$ (KPa) ²			
	Without screen	8x8 mesh screen	12x14 mesh screen	20x20 mesh screen
1.4	0.2	0.3	0.1	0.09
1.5	0.5	0.7	0.3	0.3
1.7	1.6	1.5	1.4	1.3
2.2	11.1	11.6	9.9	9.5
2.4	16.3	14.5	13.5	6.8
2.6	30.0	17.6	13	6.6
2.9	38.1	21.4	13.3	6.1
3.1	45.2	25	13.5	5.9
3.3	57.0	26.6	13.8	3.7

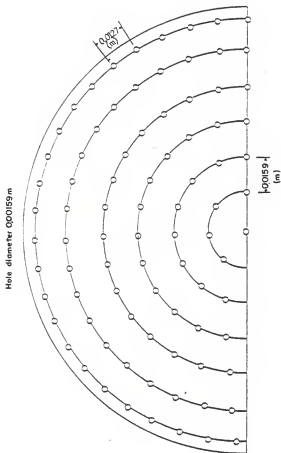


Fig. 4-2. Hole layout of the distributor.

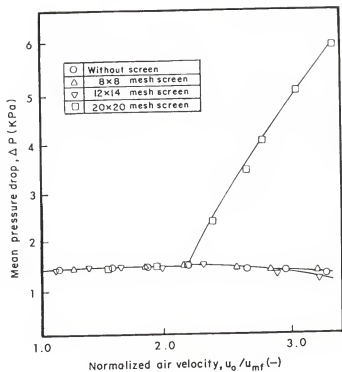


Fig. 4-3. Screen effect on the average pressure drop through the fluidized bed.

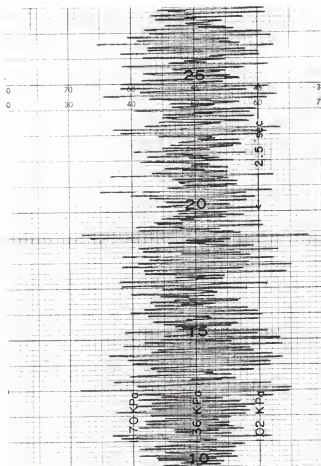


Fig. 4-4. Pressure fluctuation signal from the fluidized bed without screen at $U/U_{mf} = 3$.

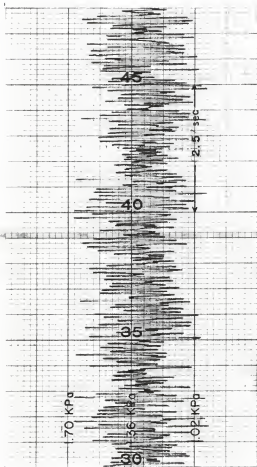


Fig. 4-5. Pressure fluctuation signal from the fluidized bed with a 8x8 mesh screen at $U/U_{mf} = 3$.

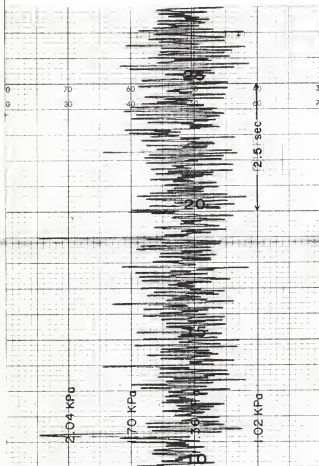


Fig. 4-6. Pressure fluctuation signal of the fluidized bed with a 12 x 14 mesh screen at $U/U_{mf} = 3$.

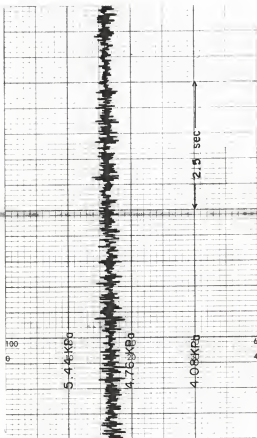


Fig. 4-7. Pressure fluctuation signal of the fluidized bed with a 20 x 20 mesh screen at $U/U_{mf} = 3$.

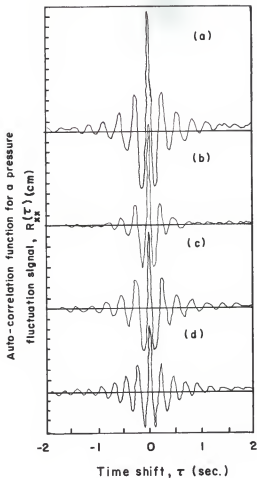
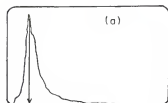


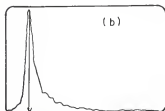
Fig. 4-8. Auto-correlation functions of the pressure fluctuation signals from the fluidized bed at $U/U_{mf} = 3.1$.

- (a) without screen
- (b) with a 8x8 mesh screen
- (c) with a 12x14 mesh screen
- (d) with a 20x20 mesh screen

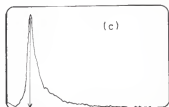
(Reproduced from the X-Y plotter; CPA attenuation = 10 dB)



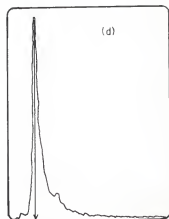
3.65
Major Frequency (Hz)



3.8
Major Frequency (Hz)



3.75
Major Frequency (Hz)



4.55
Major Frequency (Hz)

Fig. 4-9. Power spectral density functions of the pressure fluctuation signals from the fluidized bed at $U/U_{mf} = 3.1$.

- (a) without screen
- (b) with a 8x8 mesh screen
- (c) with a 12x14 mesh screen
- (d) with a 20x20 mesh screen

(Reproduced from the X-Y plotter with peak values determined by the oscilloscope cursor.)

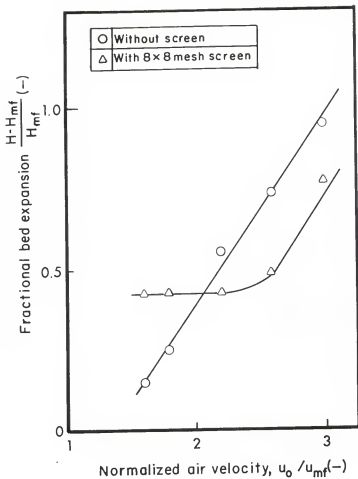


Fig. 4-10. Screen effect on the fluidized bed expansion.

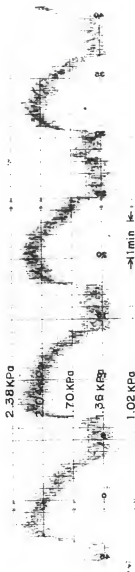


Fig. 4-11. Pressure fluctuation signal from the fluidized bed with a 20x20 mesh screen at $U/U_{mf} = 2.9$ exhibiting a periodic wave superimposed on the random fluctuations.

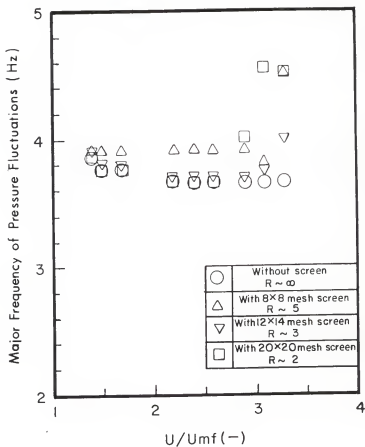


Fig. 4-12. Screen effect on the major frequency of pressure fluctuations.

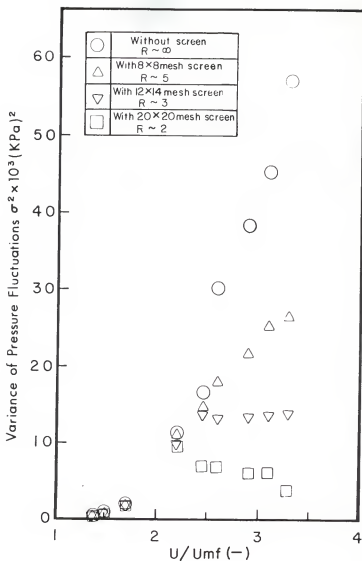


Fig. 4-13. Screen effect on the variance of pressure fluctuations.

APPENDIX A

PRE-EXPERIMENTAL CALIBRATION AND TEST RUN

Before conducting the experiment, each component in the calculation assembly was calibrated by following the instructions given in their technical manuals. In addition, the strip chart recorder and the correlation and probability analyzer needed additional calibration to correlate the results given by them in terms of voltage to those in terms of pressure

Strip Chart Recorder

In calibrating the strip chart recorder, a manometer served as a standard pressure source. Upon manipulating the manometer, the strip chart recorder recorded the signal in terms of voltage transmitted from the pressure transducer. Each voltage thus corresponded to a known pressure value. The result is shown in Fig. 4-A.1, in which the range of the strip chart recorder is set on 10V; the plot indicates that one volt on the strip chart recorder represents a pressure of 0.34 KPa.

X-Y Plotter Correlation and Probability Analyzer

The X-Y plotter plots the calculated results from the correlation and probability analyzer (CPA) in terms of voltage. A calibration procedure to interpret the plot in voltage into that in pressure is given below.

1. Set CPA into DC mode.
2. Use a zero pressure drop condition to decide the base line on the X-Y plotter.
3. Select a pressure drop by manipulating the manometer.
4. Adjust the attenuation to a value on which the OVERLOAD light on the CPA just flashes; Record the attenuation.
5. Run the CPA, and plot the calculated auto-correlation function, which should be a flat line, on the X-Y plotter. The line will be L cm above the base line.
6. Multiply L (cm) by S (mV/cm), the sensitivity of the X-Y plotter. Throughout this study, the sensitivity was set at 50 mV/cm.
7. Calculate the G value by the equation

$$G = k (LS)$$

(A-1)

where k is a constant whose value can be found in the CPA technical manual for different attenuations.

8. Plot the pressure reading from the manometer against R. The results are shown in Table 4-A.1 and Fig. 4-A.2.

To use the calibration result in determining the variance of pressure fluctuations, we must follow the procedure given below.

1. Read the function value at zero time shift of an auto-correlation function plotted by the X-Y plotter. The value, $R_{xx}(0)$, is h cm.
2. Multiply h by S.
3. Calculate the G value.

$$G = [k(hS)]^{\frac{1}{2}}$$

4. Use the calibration curve in Fig. 4-A.2 to obtain a pressure value corresponding to ().
5. Evaluate the variance by squaring the pressure value.

Test Run

A preliminary test run was carried out to determine the minimum fluidization velocity and mean pressure drop through the bed after it was fully fluidized. The result is shown in Fig. 4-A.3, illustrating that U_{mf} is 0.25 m/sec and the mean pressure drop under full fluidization is 1.35 KPa.

The data and parameters pertaining to this experiment include

$$\begin{aligned}
 D_b &= 20.3 \text{ cm} \\
 \bar{d}_p &= 0.049 \text{ cm } (-30 \sim +40 \text{ mesh}) \\
 \rho_p &= 2.6 \text{ g/cm}^3 \\
 \rho_g &= 1.16 \times 10^{-3} \text{ g/cm}^3 \text{ (air at } 35^\circ\text{C)} \\
 \mu_g &= 0.00018 \text{ g/cm sec (air at } 35^\circ\text{C)} \\
 W &= 5100 \text{ g}
 \end{aligned}$$

A theoretical value of the minimum fluidization velocity can be calculated by the Ergun equation based on the data given above (see, e.g., McCabe and Smith, 1960).

For small particles in this study, the particle Reynolds number at the onset of fluidization is

$$\begin{aligned}
 Re_p &= (33.67^2 + 0.0408 K^3)^{1/2} - 33.67 \\
 &= 5.97
 \end{aligned} \tag{A-2}$$

where K is the settling criterion defined by

$$K = \frac{d_p}{\mu} \left[\frac{g_p (n - \rho_g)}{2} \right]^{\frac{1}{2}} \quad (A-3)$$

$$= 22.06$$

For small particles with $Re_p < 20$, the minimum fluidization velocity is determined approximately by the Ergun equation as

$$u_{mf, theo.} = \frac{d_p^2 g_p (n - \rho_g)}{1650 \mu_g} \\ = 0.21 \text{ (m/sec)}$$

The experimentally obtained value is 19% greater than this estimated value.

Also, the mean pressure drop can be estimated based on the assumption that the pressure drop across the bed can mainly be attributed to the effective weight of the fluidized particle, i.e.,

$$\begin{aligned} -\Delta P &= \frac{\text{effective weight of fluidized particle}}{\text{cross-sectional area of the bed}} \\ &= \frac{W}{A} \\ &= 1.51 \text{ KPa} \end{aligned}$$

The experimentally obtained value is 15% smaller than this estimate value. Note that 15% of the fluidized particles usually rest on the dead zone immediately above the grids of the distributor, thereby not contributing to the pressure drop.

Table 4-A.1. Pre-experimental calibration data for pressure-voltage conversion in using CPA and X-Y plotter (X-Y plotter sensitivity setting = 50 mV/cm).

Run #	Manometer reading P(KPa)	CPA Attenuation (db)	L (cm)	LS (V)	k	C=k(LS) (V ²)	\sqrt{G} (V)
1	0	0	0	0	0.008	0	0
2	0.008	0	2.4	0.12	0.008	0.00096	0.031
3	0.019	0	8	0.4	0.008	0.0032	0.057
4	0.024	5	4.25	0.2125	0.02529	0.00537	0.073
5	0.020	1	8.0	0.4	0.01007	0.00403	0.063
6	0.020	0	9.6	0.48	0.008	0.00384	0.062
7	0.023	2	8.3	0.415	0.01268	0.00526	0.073
8	0.033	6	5.45	0.2725	0.03185	0.00868	0.093
9	0.04	5	8.45	0.423	0.02529	0.0107	0.103
10	0.04	4	10.8	0.54	0.01009	0.01085	0.10
11	0.04	4	10.75	0.538	0.02009	0.0108	0.104
12	0.06	7	12.2	0.61	0.04009	0.02445	0.16
13	0.066	8	9.75	0.488	0.05048	0.213	0.146
14	0.073	10	7.8	0.39	0.08	0.312	0.177
15	0.09	9	12.3	0.615	0.06355	0.03908	0.20
16	0.10	10	12.6	0.63	0.08	0.0504	0.22
17	0.11	12	10.5	0.525	0.1268	0.0666	0.258
18	0.21	15	16.5	0.825	0.2529	0.2086	0.46
19	0.26	18	13.1	0.655	0.5048	0.331	0.575
20	0.26	17	16.25	0.813	0.4009	0.326	0.571

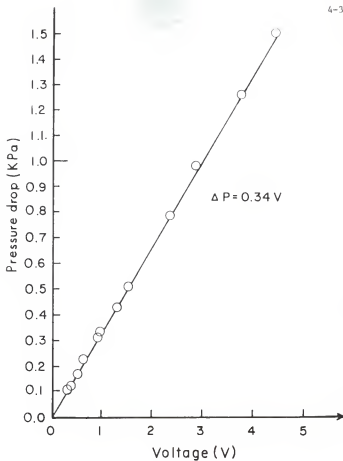


Fig. 4-A.1. Calibration curve of the strip chart recorder.

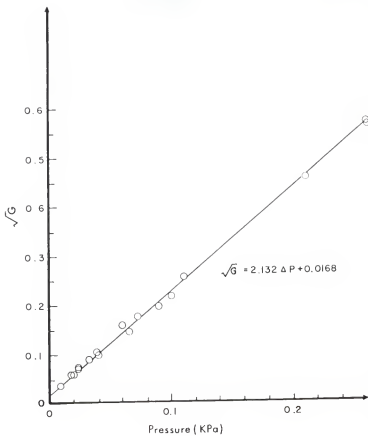


Fig. 4-A.2. Calibration curve of the X-Y plotter.

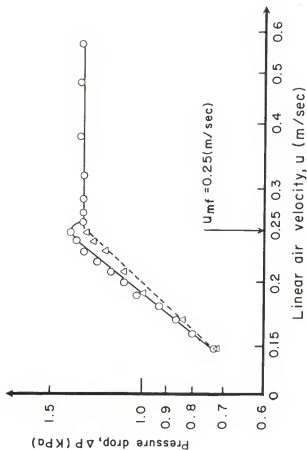


Fig. 4-A.3. Pressure drop versus linear air velocity curve for determination of the minimum fluidization velocity.

APPENDIX B

AUTO-CORRELATION FUNCTION AND POWER SPECTRAL DENSITY FUNCTION

The pressure fluctuations in a fluidized bed have been empirically verified as an ergodic process and analyzed using statistical methods by many investigators (see, e.g., Kang et al., 1967; Lirag and Littman, 1971; Fan et al., 1981). For a continuous, stationary, random process, $X(t)$, its probability function $f_{X(t)}(x)$ can be calculated as

$$f_{X(t)}(x)\Delta x = \lim_{T \rightarrow \infty} \frac{1}{T} \Sigma (\Delta T) \quad (B-1)$$

where $\Sigma(\Delta T)$ is the total time interval in which $X(t)$ falls within the narrow amplitude window (Δx) centered at a given amplitude x , and its cumulative probability distribution function is defined as

$$F_{X(t)}(x) = \int_{-\infty}^x f_{X(t)}(x) dx \quad (B-2)$$

Under the assumption of ergodicity, the mean μ and the variance σ^2 of $X(t)$ can be computed, respectively, as

$$\mu = \lim_{T \rightarrow \infty} \frac{1}{T} \int_{-\frac{T}{2}}^{+\frac{T}{2}} x(t) dt \quad (B-3)$$

and

$$\sigma^2 = \lim_{T \rightarrow \infty} \frac{1}{T} \int_{-\frac{T}{2}}^{+\frac{T}{2}} (x(t) - \mu)^2 dt \quad (B-4)$$

The auto-correlation function of $X(t)$ is given by

$$R_{xx}(\tau) = \lim_{T \rightarrow \infty} \frac{1}{T} \int_{-\frac{T}{2}}^{\frac{T}{2}} x(t)x(t+\tau)dt \quad (B-5)$$

Note that if $X(t)$ has a zero mean, $R_{xx}(0)$ defines the variance of $X(t)$. The power spectral density function $S_{xx}(\omega)$ of $X(t)$ is the Fourier transform of its auto-correlation function, i.e.,

$$S_{xx}(\omega) = \int_{-\infty}^{\infty} R_{xx}(\tau) e^{-j2\pi\omega\tau} d\tau \quad (B-6)$$

CHAPTER 5

STATISTICAL ANALYSIS OF TEMPERATURE EFFECTS ON
PRESSURE FLUCTUATIONS IN A GAS-SOLID FLUIDIZED BED

The hydrodynamic properties of fluidized beds have attracted considerable attention in recent years. A thorough knowledge of the hydrodynamic properties is recognized as a prerequisite for complete mastery of fluidization as a process technology. Most of the industrial fluidized beds are operated at temperatures higher than ambient; however, research effort in the temperature effect on the fluidized-bed hydrodynamics is relatively meager (see, e.g., Svoboda *et al.*, 1981a,b; 1983). The hydrodynamics of a gas-solid fluidized bed are characterized by random bubbling of the fluidizing gas interacting with the turbulent motion of fluidized solids. Although the behavior of bubbles and that of solids affected by it are complex and stochastic in nature, they can be described through analysis of pressure fluctuations in the bed. It has been known (Fan *et al.*, 1981) that such fluctuations are a fairly clear manifestation of behavior of bubbles and solids.

The objective of this chapter is to present the results of analyses of pressure fluctuations in a fluidized bed reactor over a wide temperature range (from room temperature to 1000K). Based on the online analysis of fluctuating signals from a pressure probe, the temperature effect on the hydrodynamics of a fluidized bed are described in detail and semi-quantitatively.

5.1 EXPERIMENTAL

The experimental facilities and procedures are presented in this section.

Facilities

Figure 5-1 is a schematic diagram of the experimental setup consisting of a fluidized bed reactor assembly, a measuring assembly and a calculating/recording assembly. The fluidized-bed reactor was originally designed to study pyrolysis and gasification of various carbonaceous material, e.g., coal, at atmospheric pressure and over a temperature range of 650K to 1450K. The reactor comprised four zones: the disengaging, the fluidized-bed, packed-bed and gas inlet zones. The reactor was constructed from a 10.16 cm (4 in.) I.D. by 55 cm (21.6 in.) length schedule 40 Inconel 600 pipe. Inconel 600 alloy was used because of its high temperature resistance and capability to withstand rapid heating and cooling. It was fitted on top with a 15.24 cm (6 in.) I.D. by 20 cm (7.9 in.) length pipe of the same material. The upper section of the reactor served as the disengaging zone or the freeboard section of the reactor.

The bottom 25 cm (9.84 in.) of the bed served as the gas distributor and preheater. The top 15 cm (5.9 in.) of this zone was packed with aluminum oxide pellets (0.5 cm in diameter). This packed-bed section allowed the fluidizing gas to be distributed uniformly in the fluidized-bed zone. The inlet zone was separated from the packed-bed zone by a 60 mesh 316 stainless steel screen (opening width = 0.23 mm; open area = 30.5%). The packed-bed and fluidized-bed zones were also separated by an identical screen. This screen prevented the filtering of the bed material into the packed-bed zone; it also influenced significantly

the characteristics of the distributor assembly.

The fluidized inert matrix was composed approximately of a mixture of 25% by weight of limestone and 75% by weight silica sand. The limestone prevented bed agglomeration which often occurs in a bed composed of sand (Walawender *et al.*, 1981). The limestone particle size was -7 to +50 mesh (2.82 to 0.287 mm); the sand particle size ranged from -30 to +50 mesh (0.595 to 0.287 mm). The bulk density of the mixture was 2.6 g/cc. The static bed height was 8 \pm 10 cm. Air was used as the fluidizing gas.

The reactor was heated by means of ten quarter cylindrical electrical resistance heaters, each capable of delivering up to 1200 watts of power with a maximum sustained operating temperature of 1500K. Voltage to each heater was controlled by three-mode, PID controllers (Omega model 49K-814). There were five chromel-alumel type thermocouples installed in the reactor. One of them, a sliding thermocouple, measured the temperature profile inside the reactor. The others were located at the freeboard, fluidized-bed section, and preheating zone and in the middle of the reactor inserted through the side wall. Three controllers recorded the temperature from these thermocouples and activated the heaters to maintain the temperature in the reactor at a pre-set value.

Figure 5-2 shows the configuration of the sliding pressure probe. It was fabricated from a hollow stainless steel pipe with a 0.32 cm I.D. and had a 0.32 x 0.64 cm² (1/8 x 1/4 in²) side hole drilled at 1.27 cm from one end. This probe had the advantage of maximally excluding the dynamic pressure from affecting the static pressure measurement. The

sliding pressure probe was installed vertically along the bed. The inside opening of the side hole, located directly above the screen distributor, was covered with a screen to prevent the fluidized particles from entering the probe. The outside opening of the probe was connected to a differential pressure transducer (Enterprise Model CJ3D, natural frequency around 5KHz), which had two input channels and produced an output voltage proportional to the pressure difference between the two input channels. In measuring the pressure fluctuations at a specific temperature, the probe was connected to the positive input channel while the other channel was left exposed to the atmosphere. The pressure transducer had a working capacity of ± 6.90 KPa (± 3 psi).

The calculating/recording assembly included a correlation and probability analyzer (Honeywell Model SAI-43A), a Fourier transform analyzer (Honeywell Model SAI-470), a strip chart recorder, an X-Y plotter, and two oscilloscopes.

Procedure

For each experimental run, the probe was placed immediately above the screen distributor; the opening of the probe was approximately 1.3 cm above the distributor. At a chosen temperature, the fluctuating signal from the probe was recorded by means of a strip chart recorder, and its auto-correlation function was calculated on-line by means of the correlation and probability analyzer. The sampling interval for this calculation was selected to be 10 ms, and a total of 16×1024 points was sampled. This led to an operating time of 164 seconds per run. The

Fourier transform analyzer transformed the auto-correlation function in the time domain into its corresponding power spectral density function in the frequency domain. The calculated results were observed on the oscilloscopes and recorded on an X-Y plotter. Experiments were repeated by changing the bed temperature, from low to high and vice versa. At a given temperature, the minimum fluidization velocity was determined graphically from the pressure vs. velocity curve obtained from the strip chart recorder.

Figure 5-3 shows an example of continuous recording of the pressure drop across the fluidized bed on the strip chart recorder; note that the fluidizing air velocity was increased stepwisely. The minimum fluidization velocity is located at point A, where the pressure drop suddenly decreases; hereafter, the pressure drop fluctuates around an essentially constant value with an increase in the air velocity. At point A, direct reading on the rotameter gives the inlet volumetric minimum fluidization velocity in standard cubic feet per minute (SCFM).

Pressure fluctuations at different normalized inlet air velocities, u_0/u_{mf} , of 1, 1.5, 2, 2.5, and 3 were recorded at various temperatures. Each datum presented is an average of those from four experimental runs with relatively small dispersion. This fact indicates that the ergodic hypothesis is validated in the present statistical analysis.

5.2 RESULTS AND DISCUSSION

Table 5-1 shows the minimum fluidization velocities, u_{mf} , under different operating bed temperatures. Table 5-2 presents the major

frequencies of pressure fluctuations in the fluidized bed (in short, the major frequencies), f_m , at different bed temperatures T and normalized inlet fluidizing air velocities, u_0/u_{mf} . Table 5-3 presents the variation of the amplitude of pressure fluctuations (in short, the amplitude), Amp , with T and u_0/u_{mf} .

Minimum Fluidization Velocity

A number of equations for predicting the minimum fluidization velocity, the air velocity at which the bed first fluidized, have been proposed (e.g., Wen and Yu, 1966). The general form of these suggested equations is

$$G_{mf} = \frac{kd \frac{\rho_g (\rho_p - \rho_g)}{\mu_g}}{\mu_g} \quad (1)$$

Assuming that the temperature effects on the particle diameter and density are negligible compared to those of the gases, eqn. (1) would predict V_{mf} and temperature to have a relationship (Desai et al., 1977).

$$\ln V_{mf} = a \ln T + b \quad (2)$$

where 'a' is a parameter reflecting the combined temperature effects on the density and viscosity of the fluidizing air; it is known that (e.g., Bird et al., 1960)

$$\rho_g \propto T^{-1} \quad (3)$$

$$\mu_g \propto T^{0.5} \quad (4)$$

from which 'a' is determined to be approximately -1.5.

Figure 5-4 shows the present experimental results in which a linear relationship of the type suggested by eqn. (2) between minimum fluidization velocity in terms of standard cubic meter per second (SCMS) and temperature (K) is observed. The slope of the line is -1.7, which is only 13% smaller than the estimated value of -1.5. Furthermore, Fig. 5-5 plots the same data in terms of linear minimum fluidization velocities at their respective temperatures. A similar trend, showing a significant temperature effect on the minimum fluidization velocity, was observed by Svoboda *et al.*, (1983), who conducted experiments using a fluidized bed with a perforated distributor.

Major Frequency of the Pressure Fluctuations

Figure 5-6 plots the major frequency given in Table 5-2 against the bed temperature with u_0/u_{mf} as the parameter. The same data are also plotted in terms of f_m vs. u_0/u_{mf} with T as the parameter in Fig. 5-7 for the low temperature range and Fig. 5-8 for the high temperature range. These plots indicate that the major frequency, normalized inlet air velocity, and bed temperature are functionally related. The following plausible mechanism can be deduced to interpret the effect of the bed temperature on the pressure fluctuations.

At a relatively low air velocity, e.g., $u_0/u_{mf} = 1$, the major frequency observed tends to increase first with temperature and then to decrease as seen in Fig. 5-6. This increase in the major frequency is expected because the increase in the bed temperature reduces the gas density and, therefore, the momentum of the air jets generated at the

distributor. The height of jet penetration thus becomes smaller and the major frequency becomes higher. Comparing this result with that reported by Knowlton and Hirsan (1980) on their study of the pressure effect on the jet penetration in a fluidized bed, we see that the response of the air jet behavior to a temperature increase is similar to that to a pressure decrease. This is a direct consequence of the property of gas. While the density of air decreases, its viscosity increases with the temperature as described in eqn. (4). When the temperature is further elevated, the decrease in the major frequency with the increase in the bed temperature can be attributed to the resultant increase in the air viscosity, thereby enhancing the stability of the flow pattern.

In contrast, at a relatively high air velocity, e.g., $u_0/u_{mf} = 3$, the major frequency tends to decrease first and then increase with the bed temperature as seen in Fig. 5-6. Notice that the velocity of $u_0/u_{mf} = 3$ is greater than the onset velocity of slugging according to the familiar criterion (Stewart and Davidson, 1967)

$$(u_{ms} - u_{mf}) \geq 0.2(0.35\sqrt{gD}) \quad (5)$$

Thus, the decrease in the major frequency at this velocity can be attributed to the decrease in the slugging frequency; this is in line with what was observed by Yamazaki *et al.* (1984) in their study of the temperature effect on the fluidized bed behavior up to 560°C. However, when the temperature exceeds this value, it is expected that the slug of air will eventually break up due to the decrease in the air density and the consequent decrease in the momentum of the slugs. The breakage of slugs results in the increase in the major frequency.

The functional relationship between the major frequency of pressure fluctuations and the bed temperature undergoes a fairly smooth transition between the two extreme cases of $u_0/u_{mf} = 1$ and $u_0/u_{mf} = 3$ explained in the preceding paragraphs.

Figures 5-7 and 5-8 show that the major frequency of pressure fluctuations is enhanced as the air velocity increases at different temperatures. The increasing tendency of the major frequency in response to the air velocity increase was also observed by Lirag and Littman (1971) at ambient temperature. Note that in both studies, a screen-type distributor was used.* The increase in the major frequency in these studies can be attributed to the fact that the rate of bubble generation at the distributor is enhanced by the increase in the air velocity. However, the major frequency can not increase without bound as the viscosity of the air in the bed increases with temperature elevation. It can be seen in Fig. 5-8 that the tendency for the major frequency to increase levels off at a certain velocity.

Amplitude of Pressure Fluctuations

The amplitude of pressure fluctuations can be regarded as an index of instability of a fluidized bed (see, e.g., Song et al., 1984). Generally

*In contrast, the major frequency of pressure fluctuations in a fluidized bed with a perforated distributor was found to decrease with the increase in the air velocity as described in Chapter 4 as well as in various other studies (see, e.g., Fan et al., 1961; Svoboda et al., 1983).

speaking, a high air velocity tends to intensify the churning in a fluidized bed that impoverishes the bed stability. This prevalent trend is shown in Fig. 5-9. It is also shown in the same figure that as temperature is elevated, the rate at which the amplitude increases with the air velocity is reduced. This is due to the fact that high viscosity at an elevated temperature enhances the stability in fluidization.

Figure 5-10 plots the same data as those in Fig. 5-9 in terms of Amp vs. T with u_0/u_{mf} as the parameter. At a low u_0/u_{mf} , e.g., $u_0/u_{mf} = 1$, the amplitude increases as temperature increases due to a reduction in fluidizing air density. On the other hand, at a high u_0/u_{mf} , e.g., $u_0/u_{mf} = 3$, the amplitude decreases with the increase in the temperature because of the increase in the viscosity.

Based on the preceding analysis, the temperature affects the fluidized-bed hydrodynamics in two major respects, namely, changing the air density and the viscosity. Moreover, it appears that the air density is a predominant factor controlling the hydrodynamic properties in the lower temperature range (e.g., temperature below 300°C) and the air viscosity becomes the prevailing factor in the higher temperature range (e.g., temperature above 300°C). This mechanism explains the concavity or convexity in Fig. 5-6, the frequency leveling-off in Fig. 5-8, the sudden slope reduction in Fig. 5-9, and the change in the slope in Fig. 5-10.

Furthermore, examination of the figures, e.g., Fig. 5-6, indicated that the discrepancy between the data and the regression lines, by fitting the polynomial curves, can not be entirely attributed to measurement error. Instead, this simply reflects the stochastic nature

of fluidized-bed hydrodynamics. It is, therefore, justifiable that only a semi-quantitative mechanism be proposed here to elucidate the effect of temperature on the fluidized-bed behavior.

NOTATION

a, b	= constants in eqn. (2)
d_p	= diameter of fluidized particles, cm
D	= diameter of the fluidized bed, cm
f_m	= major frequency of pressure fluctuations, Hz
g	= gravitational constant, g/cm^2
G_{mf}	= minimum fluidization velocity, cm/sec
k	= constant in eqn. (1), cm/sec^2
T	= temperature, $^{\circ}C$
u_0	= linear inlet air velocity, cm/sec
u_{mf}	= minimum fluidization velocity, cm/sec
u_{ms}	= minimum slugging velocity, cm/sec
V_{mf}	= minimum fluidization velocity, SCMS

GREEK LETTERS

ν_g = gas viscosity, g/cm sec

ρ_g = gas density, g/cm³

ρ_p = particle density, g/cm³

Table 5-1. Temperature effect on minimum fluidization velocity.

T (°C)	V_{mf}		u_{mf} (m/s)
	(SCFM)	(10 ⁻⁴ SCMS)	
25	1.95	9.2	0.114
52	2.0	9.4	0.126
75	1.7	8.02	0.116
115	1.58	7.43	0.118
150	1.4	6.61	0.114
163	1.25	5.9	0.106
185	1.1	5.2	0.107
270	0.8	3.78	0.085
306	0.7	3.3	0.078
400	0.5	2.36	0.069
445	0.46	2.17	0.063
530	0.43	2.03	0.067
620	0.25	1.18	0.045
700	0.25	1.18	0.049
750	0.25	1.18	0.047

Table 5-2. Temperature effect on the major frequencies of pressure fluctuations at different air velocities.

T(°C)	Major frequency (Hz)				
	$u_0/u_{mf} = 1$	$u_0/u_{mf} = 1.5$	$u_0/u_{mf} = 2$	$u_0/u_{mf} = 2.5$	$u_0/u_{mf} = 3$
25	3.13	4.42	4.72	5.15	----
52	3.54	4.1	4.57	4.68	----
75	3.85	4.68	4.05	5.41	4.78
115	3.83	4.53	4.6	5.1	4.98
185	4.1	4.33	4.55	4.12	3.95
270	4.35	4.41	4.7	4.33	4.1
306	3.78	4.98	4.4	4.45	4.2
400	3.85	4.23	4.7	4.78	4.58
445	3.05	4.08	4.6	4.33	4.6
530	3.62	4.6	4.7	4.6*	4.48
620	2.98	4.35	4.9	4.68	4.15
700	2.88	4.32	4.9	4.8	4.73

* $u_0/u_{mf} = 2.8$

Table 5-3. Temperature effect on the amplitudes of pressure fluctuations at different air velocities.

T (°C)	Amplitude (KPa)				
	$u_0/u_{mf} = 1$	$u_0/u_{mf} = 1.5$	$u_0/u_{mf} = 2$	$u_0/u_{mf} = 2.5$	$u_0/u_{mf} = 3$
25	0.0333	0.176	0.397	-----	-----
52	0.0182	0.145	0.357	0.520	-----
75	0.0329	0.173	0.316	0.482	0.608
115	0.0367	0.221	0.334	0.542	0.614
306	0.0512	0.182	0.214	0.268	0.364
445	0.0703	0.189	0.309	0.274	0.244
620	0.144	0.210	0.250	0.226	0.307

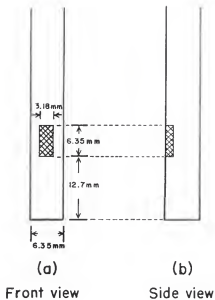


Fig. '5-2. Configuration of the pressure probe.

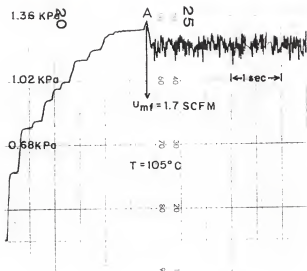


Fig. 5-3. Dynamic approach to determine the minimum fluidization velocity.

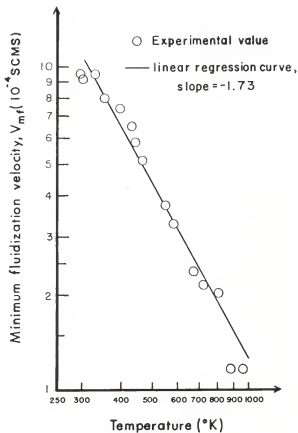


Fig. 5-4. Relationship between $\ln V_{mf}$ and $\ln T$.

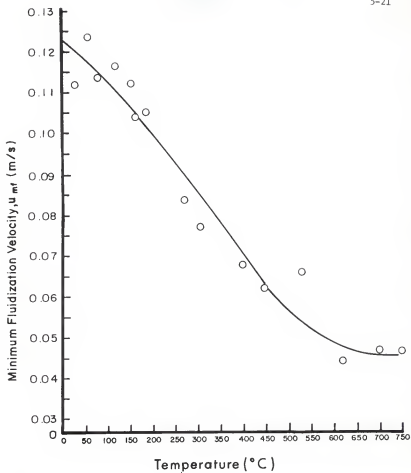


Fig. 5-5. Relationship between u_{mf} and T .

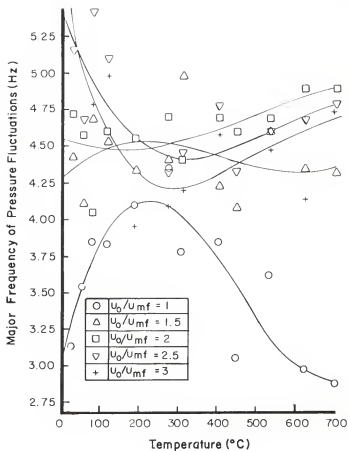


Fig. 5-6. Relationship between f_m and T with u_0/u_{mf} as the parameter.

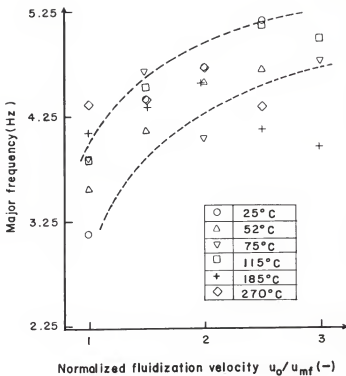


Fig. 5-7. Relationship between f_m and u_0/u_{mf} with T as the parameter (Low temperature range).

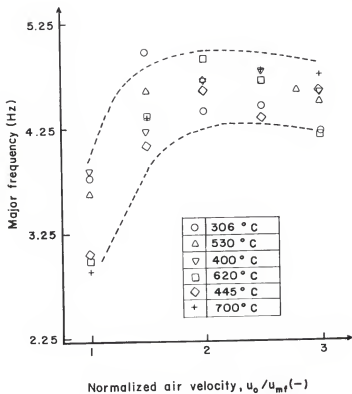


Fig. 5-8. Relationship between f_m and u_0/u_{mf} with T as the parameter (High temperature range).

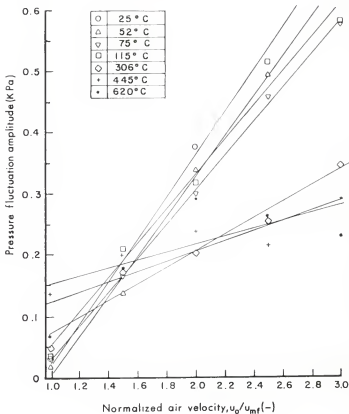


Fig. 5-9. Relationship between Amp and u_0/u_{mf} with T as the parameter.

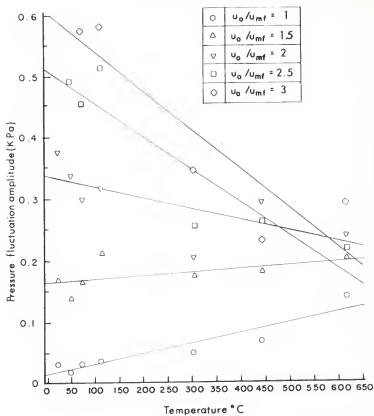


Fig. 5-10. Relationship between Amp and T with u_0/u_{mf} as the parameter.

CHAPTER 6

CONCLUSIONS AND RECOMMENDATIONS

The present study has yielded the following significant conclusions:

1. The master equation formulation has been demonstrated to be an effective approach for modeling the bubble coalescence and and breakage phenomena in a dispersed system including a fluidized bed.
2. Expansion of the resultant master equation yields a set of population balance equations (PBE's) and a set of Fokker-Planck equations (FPE's). Solution of the PBE's gives a macroscopic bubble size distribution. Equations of various moments of random variables representing fluctuations in the bubble numbers can be generated from the FPE's, from which the fluctuating components of the bubble size distribution are recovered.
3. The on-line correlation and analysis of pressure fluctuations have been shown to reveal significant stochastic features of a fluidized bed.
4. The insertion of a screen in a fluidized bed tends to stabilize the bed. In other words, the bed with a screen exhibits pressure fluctuations with a higher frequency and a smaller amplitude than an equivalent bed without a screen.
5. The insertion of a screen may cause undesirable concomitant effects such as an increase in the pressure drop and segregation of the bed. Thus, caution should be exercised in using a screen for bed stabilization.

6. When temperature increases, the density of the fluidizing air decreases, and its viscosity increases. While the resultant high viscosity tends to stabilize the bed, the reduced density tends to destabilize it. Generally, the density effect dominates at a lower temperature, e.g., temperature below 300°C, and the viscosity effect prevails at a higher temperature, e.g., temperature above 300°C.

The recommendations for future works are listed below.

1. Extension of the master equation to a fluidized-bed modeling.
A fluidized bed can be modeled as a series of compartments; each compartment is an agitated dispersed system with an overall inflow from a lower compartment and outflow to an upper one. The master equation formulation developed should be extended to this compartment model.
2. Numerical solution for the master equation. Analytical solutions are difficult to obtain for the general PBE's and FPE's resulted from the master equation expansion. It is desirable to solve them numerically.
3. Cross-correlation between signals from different positions and/or types of probes. Signals detected from different positions and/or types of probes can be cross-correlated. Examples are pressure signals across a screen and pressure signals against capacitance signals. The information obtained will provide us with a better understanding of the behavior of a fluidized bed.

Fluidized bed hydrodynamics are extremely complex and have yet to be fully understood because of the limitation in the available techniques and facilities to study them. It appears that the techniques, both theoretical and experimental, described in this thesis are especially suitable to study the stochastic phenomena of fluidized-bed hydrodynamics.

LITERATURE CITED

1. Argyriou, C. T., H. L. List and R. Shinnar, "Bubble Growth by Coalescence in Gas Fluidized Beds," *AIChE Journal*, 17, 122 (1971).
2. Bailie, R. C., D. S. Chung, and L. T. Fan, "Logitudinal Solid Density Distribution in Gas-Solid Screen Fluidized Bed," *Ind. Eng. Chem. Fund.*, 2, 245 (1963).
3. Bajpai, R. K., D. Ramkrishna, and A. Prokop, "A Coalescence Redisperison Model for Drop-Size Distributions in an Agitated Vessel," *Chem. Eng. Sci.*, 31, 913 (1976).
4. Bakker, P. J. and P. M. Heertjes, *Brit. Chem. Eng.*, 3, 240 (1958).
5. Bakker, P. J. and P. M. Heertjes, "Porosity Distributions in a Fluidized Bed," *Chem. Eng. Sci.*, 12, 260 (1960).
6. Bird, R. B., W. E. Stewart, and E. N. Lightfoot, *Transport Phenomena*, p. 21, John Wiley, New York, 1960.
7. Botterill, J. S. M., Y. Teoman, and K. R. Yuregir, "The effect of Operating Temperature on the Velocity of Minimum Fluidization, Bed Voidage and General Behavior," *Powder Technology*, 31, 101 (1982).
8. Broughton, J., "The Influence of Bed Temperature and Particle Size Distribution on Incipient Fluidization Behavior," *Trans. Instn. Chem. Engrs.*, 52, 105 (1974).
9. Bukur, D., H. S. Caram and N. R. Amundson, *Chemical Reactor Theory, A Review*, Chap. 11, 686, Prentice Hall, Englewood, NJ, 1977.
10. Coulaloglou, C. A. and L. L. Tavlarides, "Description of Interaction Processes in Agitated Liquid-Liquid Dispersions," *Chem. Eng. Sci.*, 32, 1289 (1977).
11. Desai, A., H. Kikukawa, and A. H. Pulsifer, "The Effect of Temperature upon Minimum Fluidization Velocity," *Powder Technology*, 16, 143 (1977).
12. Doheim, M. A. and C. N. Collinge, "Effect of Temperature on Incipient Fluidization and Study of Bed Expansion," *Powder Technology*, 21, 289 (1978).
13. Fan, L. T., T. C. Ho, S. Hiraoka, and W. P. Walawender, "Pressure Fluctuations in a Fluidized Bed," *AIChE Journal*, 27, 388 (1981).

14. Fox, R. and L. T. Fan, "A Master Equation Formulation for Stochastic Modeling of Mixing and Chemical Reactions in Inter-Connected Continuous Stirred Tank Reactors," To be presented at the Eighth International Symposium on Chemical Reaction Engineering, Edinburgh, Scotland, September 10-13, 1984; also to appear in the proceedings of the symposium.
15. Geldart, D. and D. S. Kapoor, "Bubble Sizes in a Fluidized Bed at Elevated Temperatures," Chem. Eng. Sci., 31, 842 (1976).
16. Ho, T. C., N. Yutani, L. T. Fan, and W. P. Walawender, "Stochastic Modeling of the Formation of Bubbles in a Shallow Fluidized Bed," Can. J. of Chem. Eng. 61, 654 (1983).
17. Hulburt, H. M. and S. L. Katz, "Some Problems in Particle Technology, A Statistical Mechanical Formulation," Chem. Eng. Sci., 19, 555 (1964).
18. Kang, W. K., J. P. Sutherland, and C. L. Osberg, "Pressure Fluctuations in a Fluidized Bed with and without Screen Cylindrical Packings," Ind. Eng. Chem. Fund., 6, 499 (1967).
19. Knowton, T. M. and I. Hirsan, "The Effect of Pressure on Jet Penetration in Semi-Cylindrical Gas-Fluidized Beds," in "Fluidization", ed. by J. R. Grace and J. M. Matsen, p. 315, Plenum Press, New York, 1980.
20. Kunii, D. and O. Levenspiel, Fluidization Engineering, John Wiley, New York, 1969.
21. Ligon, J. R. and N. R. Amundson, "Modeling of Fluidized Bed Reactors - VI (a) An Isothermal Bed with Stochastic Bubbles," Chem. Eng. Sci., 36, 653 (1981a).
22. Ligon, J. R. and N. R. Amundson, "Modeling of Fluidized Bed Reactors - VI(b). The Nonisothermal Bed with Stochastic Bubbles," Chem. Eng. Sci., 36, 661 (1981b).
23. Lirag, R. and H. Liftman, "Statistical Study of Pressure Fluctuations in a Fluidized Bed," AIChE Symp. Ser., 67 (116), 11 (1971).
24. Massimilla, L. and S. Bracale, Ricerca Sci., 26, 487 (1956).
25. Massimilla, L. and J. W. Westwater, "Photographic Study of Solid-Gas Fluidization," AIChE Journal, 6, 134 (1960).
26. Mii, T., K. Yoshida, and D. Kunii, "Temperature-Effects on the Characteristics of Fluidized Beds," J. of Chem. Eng. of Japan, 6, 100 (1973).

27. Orcutt, J. C. and B. H. Carpenter, "Bubble Coalescence and the Simulation of Mass Transport and Chemical Reaction in Gas Fluidized Beds," *Chem. Engg. Sci.* 26, 1049 (1971).
28. Prigogine, I. and I. Stengers, *Order Out of Chaos*, Chap. VI, 177, Bantam Books, New York, 1984.
29. Ramkrishna, D., "Drop-Breakage in Agitated Liquid-Liquid Dispersions," *Chem. Eng. Sci.*, 29, 987 (1974).
30. Saxena, S. C. and C. J. Vogel, "The Measurement of Incipient Fluidization Velocities in a Bed of Coarse Dolomite at Temperature and Pressure," *Trans. Instn. Chem. Engrs.*, 55, 184 (1977).
31. Shah, B. H., D. Ramkrishna, and J. D. Borwanker, "Simulation of Bubble Populations in a Gas Fluidized Bed," *Chan. Eng. Sci.*, 32, 1419 (1977).
32. Singh, B., C. R. Rigby, and T. C. Callcott, "Measurement of Minimum Fluidization Velocities at Elevated Temperatures," *Trans. Instn. Chem. Engrs.*, 51, 93 (1973).
33. Song, J. C., L. T. Fan, and N. Yutani, "Fault Detection of the Fluidized Bed Distributor by Pressure Fluctuation Signal," *Chem. Eng. Commun.*, 25, 105 (1984).
34. Stewart, P. S. B. and J. F. Davidson, "Slug Flow in Fluidized Beds," *Power Technology*, 1, 61 (1967).
35. Sutherland, J. P., C. Vassilatos, H. Kubota, and C. L. Osberg, "The Effect of Packing on a Fluidized Bed," *AIChE Journal*, 9, 437 (1963).
36. Svoboda, K. and M. Hartman, "Deviations of Actual Minimum Fluidification Velocities from Theoretical Predictions at Different Temperatures," *AIChE Journal*, 27, 866 (1981a).
37. Svoboda, K. and M. Hartman, "Influence of Temperature on Incipient Fluidization of Limestone, Lime, Coal, Ash, and Corundum," *Ind. Eng. Chem. Process Des. Dev.*, 20, 319 (1981b).
38. Svoboda, K., J. Cermak, M. Hartman, J. Drahos, and K. Selucky, "Pressure Fluctuations in Gas-Fluidized Beds at Elevated Temperatures," *Ind. Eng. Chem. Process Des. Dev.*, 22, 514 (1983).
39. Valentas, K. J. and N. R. Amundson, "Breakage and Coalescence in Dispersed Phase Systems," *Ind. Eng. Chem. fund.*, 5, 533 (1966).
40. van Kampen, N. C., *Stochastic Process in Physics and Chemistry*, North-Holland, Netherlands, 1981.

41. Walawender, W. P., S. Ganesan, and L. T. Fan, "Steam Gasification of Manure in a Fluidized Bed: Influence of Limestone as a Bed Additive," Symposium Papers: Energy from Biomass and Wastes V., Institute of Gas Technology, 517 (1981).
42. Weimer, A. W. and G. J. Quarderer, "On Dense Phase Voidage and Bubble Size in High Pressure Fluidized Beds of Fine Powders," presented in the 1983 Annual AIChE Meeting, Washington, D. C., October 31, 1983. (Paper No. 11e).
43. Wen, C. Y. and Y. H. Yu, Chem. Eng. Prog. Symp. Ser., 62, 100 (1966).
44. Winter, O., "Density and Pressure Fluctuations in Gas Fluidized Bed," AIChE Journal, 14, 426 (1968).
45. Yamazaki, R., G. H. Hong and G. Jimbo, "The Behavior of Gas-Solid Fluidized Bed at Elevated Temperatures," in "Fluidization," ed. by D. Kunii and R. Toei, p. 121, AIChE Publications Department, New York, 1984.
46. Yoshida, K., S. Fjuii, and D. Kunii, "Characteristics of Fluidized Beds at High Temperatures," in "Fluidization Technology," ed. by D. L. Keairns, 1, p. 43, McGraw Hill, 1975.

STUDIES ON THE STOCHASTIC BEHAVIOR
OF THE GAS-SOLID FLUIDIZED BED

by

YEE-WEI HUANG

B.S., National Taiwan University, 1980

AN ABSTRACT OF A MASTER'S THESIS

submitted in partial fulfillment of the

requirements for the degree

MASTER OF SCIENCE

College of Engineering

KANSAS STATE UNIVERSITY
Manhattan, Kansas

1984

ABSTRACT

The objective of this work is to study statistically and stochastically the hydrodynamics of gas-solid fluidized bed. The emphases are on the phenomena of bubble coalescence and breakage as well as the effects of the screen and the temperature on the bed performances. The master equation formulation followed by its expansion technique have been demonstrated to be an effective approach for modeling the bubble coalescence and breakage phenomena in a dispersed system including a fluidized bed. The on-line correlation and analysis of pressure fluctuations have been shown to reveal significant stochastic features of a fluidized bed including its behavior as affected by insertion of a screen or elevation of temperature.